This is a preprint submitted to EarthArxiv.
It has been accepted in Geochemistry, Geophysics and Geosystems (Jan, 2022)

Explosive activity on Kīlauea's Lower East Rift Zone fuelled by a volatile-rich, dacitic melt

Penny. E. Wieser*[1, 2], Marie Edmonds[1], Cheryl Gansecki[3], John Maclennan[1], Frances E. Jenner[4], Barbara Kunz[4], Paula Antoshechkina[5], Frank Trusdell[6], R. L. Lee[6], EIMF[7].

[1]Department of Earth Sciences, University of Cambridge, UK

[2]Now at College of Earth, Ocean and Atmospheric sciences, Oregon State University, USA

[3]Department of Geology, University of Hawai'i at Hilo, Hilo, HI 96720, USA

[4]School of Environment, Earth and Ecosystem Sciences, The Open University, MK7 6AA, UK

[5]Division of Geological and Planetary Sciences, California Institute of Technology, Pasadena, CA 91125, USA

[6]USGS Hawaiian Volcano Observatory, Hilo, HI 96720, USA

[7]Edinburgh Ion Microprobe Facility, School of Geosciences, University of Edinburgh, EH9 3JW, UK

Abstract (250 words for G3)

Magmas with matrix glass compositions ranging from basalt to dacite erupted from a series of 24 fissures in the first two weeks of the 2018 Lower East Rift Zone (LERZ) eruption of Kīlauea Volcano. Eruption styles ranged from low spattering and fountaining to strombolian activity. Major element trajectories in matrix glasses and melt inclusions hosted by olivine, pyroxene and plagioclase are consistent with variable amounts of fractional crystallization, with incompatible elements (e.g., Cl, F, H_2O) becoming enriched by 4-5 times as melt MgO contents evolve from 6 to 0.5 wt%. The high viscosity and high H_2O contents (~2 wt%) of the dacitic melts erupting at Fissure 17 account for the explosive Strombolian behavior exhibited by this fissure, in contrast to the low fountaining and spattering observed at fissures erupting basaltic to basaltic-andesite melts. Saturation pressures calculated from melt inclusions CO_2-H_2O contents indicate that the magma reservoir(s) supplying these fissures was located at ~2-3 km depth, which is in agreement with the depth of a dacitic magma body intercepted during drilling in 2005 (~2.5 km) and a seismically-imaged low Vp/Vs anomaly (~2 km depth). Nb/Y ratios in erupted products are similar to lavas erupted between 1955-1960, indicating that melts were stored and underwent variable amounts of crystallization in the LERZ for >60 years before being remobilized by a dike intrusion in 2018. We demonstrate that extensive fractional crystallization generates viscous and volatile-rich magma with potential for hazardous explosive eruptions, which may be lurking undetected at many ocean island volcanoes.

Plain Language Summary

During the first two weeks of the 2018 eruption of Kīlauea Volcano, Hawai'i, a wide variety of magma compositions were erupted from 24 separate fissures. Of particular interest is the magma erupted at Fissure 17, which was much more explosive than nearby fissures, throwing large pieces of molten rock several hundred metres into the air, causing a serious injury. The explosivity of volcanic eruptions is partially controlled by the viscosity of the magma (how easily it can flow), and partially by the amount of dissolved H_2O and CO_2 (which exsolve like bubbles in a carbonated beverage as the melt ascends to the surface). We show that melts erupted at Fissure 17 were significantly more viscous and H_2O-rich than the melts erupted more passively at nearby fissures. These two factors account for the explosive eruptive style of this fissure. Using the relationship between the amount of

dissolved H_2O and CO_2 and pressure, we show that erupted magmas were stored at ~2km depth below the surface since at least 1955-1960 A.D.

Key points (140 characters)

1. The first 2 weeks of the 2018 Kīlauea eruption tapped melts undergoing variable amounts of fractionation at ~2-3 km depth over >60 yrs.
2. Saturation pressures calculated from melt inclusion volatile contents align with the depth of a seismically imaged Vp/Vs anomaly.
3. The strombolian explosions at Fissure 17 result from the high viscosity and the high H_2O contents of these dacitic melts

1. Introduction

The main shield-building stage of volcanism at ocean island volcanoes fed by high melt fluxes from mantle plume melting (e.g., Hawai'i, Galápagos, Réunion) is characterized by the eruption of basaltic lava flows, spatter, and occasional energetic lava fountains (Macdonald, 1962; Swanson et al., 1979). On a number of occasions at Kīlauea Volcano, HI, erupted basaltic lava has pooled within existing pit craters, undergoing extensive fractional crystallization at near atmospheric pressures (e.g., 1959 Kīlauea Iki lava lake, 1963 Alae lava lake, 1965 Makaopuhi Crater; Helz, 1980; Wright et al., 1976). It is becoming increasingly apparent that andesitic to rhyolitic melts analogous to those formed in surface lava lakes may also co-exist with basaltic melts at depth within a range of volcanic plumbing systems, even if these more silicic compositions are poorly represented in erupted rock compositions (Stock et al., 2020). The first detailed description of such lavas from the shield stage of a Hawaiian volcano was provided by Bauer et al., (1973), who investigated a rhyodacite from the late shield stage from the Kaua'ōpu'u ridge of Oahu. In 2005, a hydrothermal injection well on Kīlauea's Lower East Rift Zone (LERZ) intercepted a stored body of dacitic magma (with a bulk composition of 67 wt% SiO_2; Teplow et al., 2009). More recently, examination of lava and tephra samples from the 2015 eruption of Wolf Volcano and the 1968 eruption of Fernandina in the Galapagos identified plagioclase crystals whose compositions indicate that they grew from basaltic trachy-andesite and trachy-andesitic melts (Stock et al., 2020).

In contrast to these tantalizing glimpses of more silicic melts in basalt-dominated ocean island volcanic settings, the first two weeks of the 2018 Lower East Rift Zone (LERZ) eruption of Kīlauea Volcano produced significant volumes of lava spanning basaltic to andesitic bulk compositions from 24 different fissures (Fig. 1b, Gansecki et al., 2019). Importantly, while lava lakes act as excellent natural laboratories to investigate major element evolution of Kīlauea magmas during differentation, because the pooling magmas have already degassed the majority of their volatiles, they do not provide representative insights into volatile element evolution within the plumbing system (Wieser et al., 2020). The eruption of melts with a wide range of bulk compositions at the surface, combined with rapid-response sampling of quenched spatter and tephra before it was covered by later lava flows (Gansecki et al., 2019), provides an unprecedented opportunity to investigate the pre-eruptive processes producing SiO_2-rich magmas from ocean island basalts, such as the depth and longevity of magma storage and differentiation, and the effect of melt composition on eruption style.

One fissure, named Fissure 17 (F17) produced highly explosive Strombolian style activity, launching 2-3 m pieces of spatter ~125 m in the air (see https://www.youtube.com/watch?v=WXcV6WqvDYs&t=108s; Supporting Video 1). These explosive outbursts caused a severe injury when spatter was thrown 150 m from the vent and shattered the leg of a resident on a third floor balcony. F17 also exhibited gas venting and the generation of shock

waves, audible in the town of Mountain View >20 km to the NW. This 3xplosive eruption style at F17 contrasted with the low-moderate fountaining (heights 30 to 80 m) and less energetic spattering observed at nearby fissures, and even the eastern end of F17 (Fig. 1d-e). F17 is offset ~220 m to the north-east of the linear trend defined by the other early eruptive fissures (Fig. 1b), and rapid-response petrological monitoring during the eruption indicated that the western, more explosive end of F17 was tapping a more SiO_2-rich composition than the eastern, less explosive end (Gansecki et al., 2019). However, the cause of the higher explosivity remains uncertain; it has been suggested that explosivity might result from the involvement of groundwater, or the higher viscosity of these more SiO_2-rich melts (Gansecki et al., 2019; Soldati et al., 2021).

Here we utilize the major, trace element and volatile element contents of olivine, pyroxene and plagioclase-hosted melt inclusions to investigate three questions:

1) What was the cause of the high explosivity observed in the eruptions at the western end of F17?
2) What was the most probable parent magma(s) of the variable melt compositions erupted in the first few weeks of the 2018 eruption?
3) At what depth were these magmas stored in the LERZ?

We show that fissures erupting in the first few weeks of the 2018 eruption tapped a stored magma body which experienced variable amounts of fractional crystallization at 2-3 km depth. Based on a comparison of incompatible trace element ratios from 2018 samples and historic activity in this section of the LERZ, we show that the 2018 eruption tapped a magma body with very similar chemistry to that supplying the 1955 and 1960 eruption. The large amounts of fractional crystallization experienced by dacitic melts erupted at F17 drove up melt H_2O contents to unprecedented levels at Kīlauea (~2 wt%) which, combined with an increase in melt viscosity, accounts for the explosive activity observed at this fissure.

1.1 Chronology of the 2018 LERZ eruption

The 2018 LERZ eruption marked the end of a 35-year-long period at Kīlauea Volcano during which activity was focused predominantly at the Puʻuʻōʻō vent, on the Middle East Rift Zone (the name change from PuʻuʻŌʻō signifies that the eruption has ended; Hawaiʻi Board on Geographic Names). Following inflation of the summit and Puʻuʻōʻō during March and April 2018 (Neal et al., 2018; Patrick et al., 2020), Puʻuʻōʻō vent collapsed on April 30th, accompanied by the propagation of a dike downrift into the Leilani Estates subdivision on the Lower East Rift Zone (LERZ). Following the formation of ground cracks, the first eruptive fissures opened on May 3rd. Fourteen additional fissures opened along a linear trend in the first week (F1 to F15; Fig. 1b). These first fissures, classified as Early Phase 1 by Gansecki et al., (2019), were characterized by whole-rock compositions with ~4-5 wt% MgO, erupted as relatively small-volume spatter mounds and lava flows. These lavas are thought to represent material which was intruded during previous eruptive episodes in the Lower East Rift Zone (e.g., 1790, 1840, 1955 or 1960 A.D; Gansecki et al., 2019; Fig. 1c). The injection of the dike beneath the Leilani Estates subdivision at the start of May, 2018, is thought to have disturbed these resident melts and forced them to the surface (e.g., by increasing overpressure, changing the crustal stress state, or thermal rejuvenation).

Following an eruptive pause, activity recommenced on May 12th-18th (termed Late Phase 1), with more fissures opening up along the same linear trend (Fissures 16, 18, 20, 22). These later fissures erupted higher magma compositions with higher bulk MgO contents (5-6 wt% vs. 4-5 wt% in Early Phase 1),which have been interpreted to represent mixing between the early rift-stored component, and the more MgO-rich magma supplied by the dike (Gansecki et al., 2019). Between the 17-27th of

May (Phase 2) effusion rates increased and whole-rock MgO contents increased again to become very similar to those erupted at Pu‘u‘ō‘ō vent (6-7 wt%), indicating that the vast majority of melts stored in the LERZ had been flushed from the system (Gansecki et al., 2019; Neal et al., 2018; Patrick et al., 2019). In addition to this general progression from relatively MgO-poor to MgO-rich melt compositions, F17 (active 13-25th of May, offset to the NE of the other fissures) erupted magma with significantly lower MgO and higher SiO_2 contents (including andesitic bulk compositions), which is thought to represent a third, stored magmatic component (Gansecki et al., 2019).

By the 28th of May (Phase 3), activity had focused at a single fissure (F8, recently renamed Ahu‘ailā‘au) which developed a fast-flowing lava channel, and erupted material with even higher bulk MgO contents resulting from the incorporation of antecrystic olivine crystals(Fig. 2a; Gansecki et al., 2019; Wieser et al., 2021b). For brevity, to distinguish between this main phase of activity at Ahu‘ailā‘au (F8), and the earlier, more MgO-poor material, we refer to activity in early Phase 1, Late Phase 1 and Phase 2 as “early fissures”, and activity at Ahu‘ailā‘au after May 28th as Phase 3.

It has been suggested, based on the presence of high forsterite olivines incorporated within Phase 3 lavas, and the bimodal distribution of melt inclusion saturation pressures at 1-2 and 3-5 km, that this magma originated from the two magma reservoirs identified by geophysical imaging beneath Kīlauea’s summit (Wieser et al., 2021, Lerner et al., 2021), with a hydraulic connection linking these reservoirs to Ahu‘ailā‘au (Gansecki et al., 2019; Neal et al., 2018; Patrick et al., 2019). Conversely, Pietruszka et al. (2021) suggest that major and trace element differences between Phase 3 lavas and those erupted at Kīlauea’s summit and Pu‘u‘ō‘ō prior to the onset of the 2018 eruption rules out a summit origin, and instead suggest that this MgO-rich magma had accumulated in the Middle East Rift Zone (MERZ) downrift of Pu‘u‘ō‘ō over ~10 years prior to 2018. The exact source of Phase 3 magma is beyond the scope of this study, which focuses on the early phase lavas erupted between May 3rd to May 16th, so we refer to Phase 3 magma as “dike-supplied” to avoid ambiguity.

2. Methods

2.1 Analytical methods

Spatter, reticulite and lava samples were collected from 9 separate fissures (Fissures 4, 5, 8, 10, 11, 12, 13, 17, and 20) on Kīlauea’s LERZ during the 2018 eruption and a follow-up field campaign in 2019 (Supporting Table S1). Care was taken to select the most rapidly-quenched water and air-quenched material to minimise H^+ diffusion out of melt inclusions (Gaetani et al., 2012). Specifically, we selected the smallest and most visibly glassy clasts available in each location. Clast size was 0.5-8 cm and water-quenched material was favoured where available. Samples were jaw-crushed, and olivine, orthopyroxene, clinopyroxene, and plagioclase crystals were picked under a binocular microscope. Crystals were individually mounted on glass slides using Crystalbond and ground down to the level of target melt inclusions. Care was taken to prioritize melt inclusions not visibly connected to the outside of the crystal, but particularly in plagioclase-hosted melt inclusions, it was often difficult to determine the degree of connectivity due to complex melt networks. An indication of whether each melt inclusion was fully isolated or connected to the carrier melt is provided in Supporting Dataset S1.

All vapour bubbles within melt inclusions were analysed for CO_2 using Raman spectroscopy following the methods described by Wieser et al., (2021). Unlike the olivine-hosted melt inclusions erupted in the Phase 3 between 28th May and Aug 1st, none of the vapour bubbles in melt inclusions from the early fissures (3rd-16th May) investigated in this study produced measurable CO_2 peaks, indicating that the concentration of CO_2 in their vapour bubbles were below the detection limit of Raman

Spectroscopy (~0.02 g/cm^3; Wieser et al., 2021). Following exposure of a target melt inclusion at the surface, crystals were mounted in epoxy stubs in groups of 30-40 inclusions, and polished using progressively finer diamond pastes.

Samples were analysed for H_2O, CO_2, F (as well as MgO and SiO_2 for normalization) using the Cameca IMS-7f GEO at the NERC Ion Microprobe Facility at the University of Edinburgh in two analytical sessions (July 2019, January 2020). A variety of glass standards were analysed with a range of Si contents to convert counts to element concentrations, and to account for matrix effects on ion yields as a function of melt SiO_2 content. Detailed analytical information is available in the Supporting information (Supporting Fig. S1-S2, Supporting Table S2).

Following SIMS analysis, the Au coat was removed by polishing on a 1 µm pad (which also helped to reduce the size of SIMS pits and remove SIMS sputter) and a C coat was applied. Matrix glasses, melt inclusions, and the composition of the mineral host ~30-100 µm away from each melt inclusion were analysed using a Cameca SX100 EPMA at the Department of Earth Sciences, University of Cambridge following the analytical techniques described in Wieser et al., (2021) (also see Supporting Text 1, Table S3-S9). Care was taken to analyse away from the SIMS pit where possible.

Trace elements were measured in melt inclusions and matrix glasses using a Photon Machines G2 193 nm excimer laser system equipped with a HelEx II 2-volume cell coupled to an Agilent 8800 ICP-MS/MS) at the School of Environment, Earth and Ecosystem Sciences, The Open University. Depending on the size of the melt inclusion and the number of microlites in matrix glasses, ablation spots were between 20 and 50 µm. Analyses were conducted following the techniques described by Jenner et al., (2015) and Wieser et al., (2020). Comparison of measurements of BCR-2G run as secondary standard to long-term laboratory preferred values is shown in Supporting Dataset S2.

2.2 Correction for Post-Entrapment Crystallization

Olivine-hosted melt inclusions were corrected for the effects of post-entrapment crystallization (PEC) using the "Olivine MI" tool in Petrolog3.1.1.3 (Danyushevsky and Plechov, 2011), which requires users to enter the measured major element composition of the melt inclusion, the host Fo content (both taken from EPMA analyses), and an estimate of the initial FeO_t content of the melt inclusion prior to post-entrapment crystallization. The initial FeO_t content was estimated by determining a relationship between olivine Fo content and melt FeO_t contents by calculating the equilibrium olivine Fo content for co-erupted matrix glasses (see Supporting text 2, Fig. S3). While olivine-hosted melt inclusions erupted in the later stages of F8 (28th May-1st Aug) have experienced up to 35% PEC (Wieser et al., 2021), the maximum amount of PEC experienced by olivines erupted at the earlier fissures examined in this study is 10% (median= 4%).

Unlike for olivine, there is no clear consensus as to the best way to reconstruct orthopyroxene, clinopyroxene, and plagioclase-hosted melt inclusion compositions for the effects of PEC. We discuss the approach taken in this study in detail in Supporting Text S2. Briefly, for clinopyroxene we examine the degree of disequilibrium between each melt inclusion and its host clinopyroxene crystal using the four equilibrium tests described by Neave et al. (2017): K_D^{Fe-Mg}, Di-Hd, En-Fs and CaTs. Melt inclusions lie within the equilibrium field for all parameters except K_D^{Fe-Mg} (Fig. S4, likely resulting from the fact that the concentration of FeO and MgO are far more sensitive than other major elements to the crystallization of small amounts of clinopyroxene on the wall of the melt inclusion). If a melt inclusion has crystallized clinopyroxene on its walls, the composition of that clinopyroxene must be added back into the measured melt inclusion composition to restore the composition at the time of entrapment. Similarly, if the inclusion was heated up and clinopyroxene

dissolved following entrapment, that clinopyroxene must be removed from the measured inclusion composition. We add/subtract the composition of the host clinopyroxene until the melt inclusion and host crystal are in K_D^{Fe-Mg} equilibrium (using Equation 35 of Wood and Blundy, 1997). The median amount of clinopyroxene addition needed to obtain K_D^{Fe-Mg} equilibrium was 4 wt% (1σ=5%; Supporting Fig. S5). Corrected melt inclusion compositions meet all four equilibrium tests, and lie closer to major element trajectories defined by co-erupted matrix glasses than uncorrected compositions (Supporting Fig. S4-S5).

Many orthopyroxene-hosted melt inclusions also lie out of K_D^{Fe-Mg} equilibrium with the composition of the host crystal (Supporting Fig. S6). However, unlike for clinopyroxene, adding/subtracting the composition of the host crystal to reach K_D^{Fe-Mg} equilibrium results in a worse fit to the major element trajectories defined by matrix glasses in CaO, and TiO_2 vs. MgO space (Supporting Fig. S7). Given that most orthopyroxene-hosted melt inclusions lie close to the major element trajectory of matrix glasses, we leave their compositions uncorrected.

The vast majority of plagioclase-hosted melt inclusions lie very close to the compositional trend defined by matrix glasses, with the exception of 6 melt inclusions erupted at F17, which are offset to significantly higher FeO (Fig. 2b) and lower CaO contents at ~6 wt% MgO (Supporting Fig. S8). These offsets are indicative of crystallization of ~15 wt% plagioclase on the walls of the melt inclusion following entrapment, likely due to extensive cooling between the formation of these relatively high anorthite crystals (~An_{60}) and their incorporation in the significantly cooler F17 melt composition (in equilibrium with ~An_{45-50}). These six melt inclusion compositions were corrected by adding the composition of the host crystal back into the measured melt inclusion composition to obtain the best fit to matrix glass data in MgO vs. Al_2O_3 space (Supporting Fig. S9). All other plagioclase-hosted melt inclusions were left uncorrected.

3. Results

3.1 Major and Volatile Elements

The composition of melt inclusions and matrix glasses erupted between May 3rd and 16th define coherent trends in major element space, spanning basaltic to dacitic compositions (~7 to 0.5 wt% MgO, 48 to 68 wt% SiO_2; Fig. 2a). The compositions of matrix glasses are distinctly clustered, with the largest group at ~4 wt% MgO (erupted at F4, F5, F8, F10-12 during Early Phase 1 on May 3-9th), a second cluster at ~1 wt% MgO (erupted at F17 on May 14th), and a third cluster at ~6-7 wt% MgO erupted in Phase 3 at Ahu‘ailā‘au (F8) after May 28th. Lavas erupted from F13 following its re-activation (F13-react) plot between the Early Phase 1 and F17 cluster, while lavas erupted at F20 on May 16th plot between the Early Phase 1 cluster and the higher MgO Phase 3 cluster. As above, we refer to early Phase 1 fissures (F4, F5, F8, F10-12), F13-react, F17 and F20 as early fissures (3rd-16th May) to distinguish them from the more MgO-rich material erupted at Ahu‘ailā‘au (F8) after May 28th in Phase 3.

Melt inclusion and matrix glass Cl and F concentrations increase with decreasing melt MgO contents, with the most volatile-rich dacitic melt inclusions erupted at F17 having Cl and F concentrations of ~1000 ppm (3-5 times higher than observed in melt inclusions erupted in phase 3; Fig. 3a-b). F concentrations show significantly more scatter than Cl concentrations. The upper limit of melt inclusion H_2O contents also increases with fractional crystallization, reaching 1 wt% in the early Phase 1 lavas with ~4 wt% MgO, and up to 2 wt% in melt inclusions erupted at F17 with 0.5-1 wt% MgO (Fig. 3d). These F17 measurements greatly exceed the highest H_2O content measured in melt inclusions from historic eruptions at Kīlauea (~1 wt% H_2O, Sides et al. 2014). Unlike Cl, F, H_2O and Zr

(Fig. 2d , Fig. 3a-c), melt inclusion CO_2 concentrations are approximately constant between 4 and 6 wt% MgO (with a maximum concentration of ~300-400 ppm), then decline slightly with decreasing MgO to ~200 ppm at 0.5-1 wt% MgO (Fig. 3c).

3.2 Trace elements

As discussed further in section 4.4, Nb/Y is not extensively fractionated during crystallization at Kīlauea, so can be used to identify distinct magma batches (Pietruszka et al., 2021). Early Phase 1 matrix glasses from F4, F5, F8, F10-12 (green symbols) have Nb/Y ratios of ~0.6-0.8, which overlap with the composition of matrix glasses erupted at F17 (Fig. 4a). In contrast, matrix glasses erupted at F13 following its reactivation and F20 have lower Nb/Y ratios, plotting closer to the composition of Phase 3 glasses. Overall, the trends defined by matrix glasses measured by LA-ICP-MS in this study are very similar to those determined by whole-rock XRF measurements (Pietruszka et al., 2021, magenta dots, Fig. 4a).

Unlike the temporal variations seen in matrix glass and whole-rock trace element compositions, there are no apparent inter-sample differences in the Nb/Y ratios of melt inclusions erupted from early fissures, or relationships between Nb/Y ratios and host crystal An# or Mg# in these samples (Fig. 4c-d). As for matrix glasses, the vast majority of melt inclusions from Phase 3 (orange colors; Fig. 4c-d) lie to distinctly lower Nb/Y ratios, with only a small number of melt inclusions erupted on May 28th overlapping with the Nb/Y ratios of melt inclusions from early fissures (particularly those hosted in lower forsterite olivines).

4. Discussion

4.1 Modelling Fractional Crystallization

The coherent trends in major and volatile element trajectories defined by melt inclusions and matrix glasses indicate that the dominant cause of chemical variability in erupted melts during the first two weeks of the 2018 eruption was fractional crystallization. Previous studies have shown that Kīlauea melts fractionate only olivine (+minor Cr-spinel) at >6.8 wt% MgO, defining a relatively flat trajectory for all elements vs. MgO (Wright and Fiske, 1971). Next, clinopyroxene joins the liquidus, followed by plagioclase after only 5-15 °C cooling, as well as minor orthopyroxene (Helz and Wright, 1992). The crystallization of plagioclase accounts for the rapid increase in melt FeO_T as MgO contents drop from 6 to 4 wt% (Fig. 2b). The appearance of plagioclase and clinopyroxene on the liquidus also causes the slope of relatively incompatible elements like TiO_2 and Zr vs. MgO to greatly increase, because a larger mass of solid is fractionated for a given decrease in melt MgO content. At ~4 wt% MgO, Fe-Ti oxides saturate (Helz and Wright, 1992), driving the concentration of FeO_T and TiO_2 down, and SiO_2 up. Concurrently, P/Nd begins to decline (along with P_2O_5; Supporting Fig. S10), indicating the onset of apatite crystallization (visible as microphenocrysts in matrix glasses from F17).

Fractional crystallization models were run using alphaMELTS for MATLAB (Rhyolite melts V1.2.0, Antoshechkina and Ghiorso, 2018; Ghiorso and Gualda, 2015; Gualda et al., 2012) to recreate observed major element trends. Although it is likely that the melt fractionating within the LERZ was a previously stored component, the starting composition of models was set as the average major-element composition of glasses erupted in Phase 3. This is because the vast majority of literature data for previous eruptions comprises whole-rock compositions, which may be affected by crystal addition. The starting composition used for the modelling lies within the range of whole-rock compositions from various early fissures from Gansecki et al. (2019), justifying this choice. The initial Fe^{3+}/Fe_T ratio was set at 0.15 (Lerner et al., 2021; Moussallam et al., 2016), and models were run without a buffer, allowing for changes in oxidation state following Fe-Ti oxide saturation. The

pressure was set at 650 bars, based on the upper range of saturation pressures measured in Early Phase 1 melt inclusions (see section 4.5). The trajectory of trace and volatile elements during fractional crystallization was modelled using the mass of solid phases produced, and the fractional crystallization equation ($C_{final}=C_{initial}*F^{D-1}$, where F is the amount of melt remaining, and D is the bulk partition coefficient).

In detail, we consider two separate model trajectories in MELTS. Model A (red line) was run with an initial H_2O concentration of 0.1 wt%. Model A is a good match to the trajectory of major elements from ~6.8 to 4 wt% MgO, capturing the sharp increase in FeO_t and TiO_2 contents with decreasing MgO. At lower MgO contents, Model A is a good fit to FeO_t, TiO_2 and SiO_2 (Fig. 2a-c) but overestimates CaO, and underestimates Al_2O_3 (Supporting Fig. S11) indicating that the ratio of clinopyroxene vs. plagioclase fractionating in this model is incorrect. Similarly, Model A does not recreate the prominent downtick in P_2O_5 (and P/Nd) caused by apatite crystallization, because MELTS currently only accounts for a hydroxy-apatite phase (rather than the more stable fluorapatite observed in natural magmas; Rooney et al., 2012). The failure to correctly model apatite saturation may also account for some of the overestimation of melt CaO contents at <4 wt% MgO (Supporting Fig. S11). However, despite these major-element discrepancies, the concentration of Zr and Cl (assuming complete incompatibility) in Model A provides a good fit to the composition of melt inclusions and matrix glasses. This indicates that MELTS model results are accurately predicting the amount of solid being fractionated, even if predictions of relative phase proportions are slightly inaccurate.

If MELTS models are initialized with water contents similar to those in melt inclusions with ~6 wt% MgO (H_2O_i=0.5 wt%, Model B, Fig. 2, dashed black lines), MELTS saturates Fe-Ti oxides significantly earlier and plagioclase later than Model A, such that Model B fails to achieve the prominent TiO_2 and FeO enrichment seen in erupted glass compositions. This has been noted previously for Kīlauea by Garcia (2003). Fortunately, the total mass of solids predicted by model A and model B are reasonably similar, so these models predict similar trajectories for incompatible elements such as Zr (Fig. 2d). We also generate a 3rd major element path for fractional crystallization, using MELTS model A at >4 wt% MgO, and a best fit through measured glass and melt inclusion data for <4 wt% (Supporting Fig. S11). The major element differences between these three models have a relatively small effect on volatile solubility (Supporting Fig. S12) and calculations of melt viscosity (Fig. 5b). This justifies the use of Model B to investigate changes in volatile systematics and viscosity during fractional crystallization, even though this model doesn't fully recreate the observed major element systematics (Fig. 2).

Rhyolite-MELTS V1.2.0 fails to reproduce olivine-only fractionation at >6.8 wt% MgO, so this section of the fractionation path was modelled using the "reverse crystallization" (RFC) tool in Petrolog3 (Danyushevsky and Plechov, 2011) from the specified starting composition.

4.2 Volatile Element Evolution during Crystallization

MELTS modelling demonstrates that the prominent enrichment in melt inclusion Cl concentrations with decreasing MgO results from extensive fractional crystallization (Fig. 3a). F data shows significantly more scatter than Cl (Fig. 3b), but approximately follows the fractional crystallization trend. Notably, six plagioclase-hosted F17 melt inclusions with higher MgO contents (~4-6 wt%) lie significantly above the fractional crystallization line for F, indicating that these inclusions may have diffusively re-equilibrated with the significantly more F-rich carrier melts in which they were erupted (Fig. 3b). Apparent open-system behavior of F in olivine-hosted melt inclusions has been noted previously by Koleszar et al., (2009) and Portnyagin et al. (2008), while Neave et al. (2017) attribute F

enrichment in plagioclase-hosted melt inclusions to diffusive pile up during rapid growth. We favour diffusive re-equilibration here, because many F17 melt inclusions have lower F contents than co-erupted matrix glasses, and it is only the most MgO-rich melt inclusions which are expected to have equilibrated with more F-rich, MgO-poor melts that show notable enrichment above the fractional crystallization trend. Two of these melt inclusions also show elevated H_2O contents (Fig. 3d), which is consistent with these more primitive melt inclusions equilibrating with the more MgO-poor, F- and H_2O- rich F17 carrier melt prior to eruption (with F re-equilibration appearing to occur faster than H_2O re-equilibration in plagioclase).

Accounting for these complexities with F, the relative similarity of the trajectories of matrix glasses and melt inclusions indicates that the amount of F and Cl degassed upon eruption is sufficiently small that it cannot be resolved petrologically by comparing melt inclusions and matrix glasses. In contrast, H_2O and CO_2 degas strongly upon eruption, shown by the significantly lower concentrations in matrix glasses relative to melt inclusions (Fig. 3c-d).

The upper limit of melt inclusion H_2O contents is bracketed by treating H_2O as an incompatible element in MELTS model A, with a number of melt inclusions plotting to lower H_2O contents. In contrast, melt inclusion CO_2 contents show a slight decline with decreasing MgO contents, again with a lot of scatter. The evolution of H_2O-CO_2 is significantly more complicated than elements like Zr and Cl, because Kīlauea melts are saturated in a mixed H_2O-CO_2 fluid at crustal pressures (Gerlach et al., 2002). This means there is a competing influence between their incompatible behavior in solid phases and their loss to an exsolving fluid phase. To demonstrate this trade-off, we use the solubility model MagmaSat (Ghiorso and Gualda, 2015) implemented in the Python3 tool VESIcal (Iacovino et al. 2021) to calculate the solubility of pure-CO_2 fluids and pure-H_2O fluids at 650 bars for the synthetic major element path which provides the best fit to measured glass and melt inclusion data (Supporting Fig. S11), using temperatures from the MgO geothermometer of Helz and Thornber, (1987). At low pressures where non-ideality between H_2O-CO_2 is negligible, the concentration of either volatile species will not exceed the pure solubility limit. The solubility of pure CO_2 is relatively low (~400 ppm), and plots close to the measured CO_2 contents of melt inclusions (dashed blue line, Fig. 3c). In contrast, the solubility of pure H_2O is much higher, plotting significantly above the concentration of melt inclusions (dashed blue line, Fig. 3d).

In reality, H_2O-CO_2 exsolves as a mixed fluid in magmatic systems. At the low pressures considered here, where mixing between H_2O and CO_2 is close to ideal, the behavior of mixed fluids is best understood considering Henry's Law (Lowenstern, 2001). Namely, the addition of H_2O to a pure CO_2 fluid lowers the partial pressure of CO_2, and therefore lowers its solubility in the co-existing melt phase. Similarly, adding CO_2 to a pure H_2O fluid lowers the solubility of H_2O in the melt. The solubility of H_2O-CO_2 in equilibrium with a mixed fluid during fractionation can be simulated in alphaMELTS for MATLAB along the fractionation path of MELTS model B (which has realistic initial H_2O contents). From 6 to 4 wt% MgO, when the melt is relatively H_2O -poor, the composition of the exsolved vapour phase (X_{CO2}) is >90 wt% CO_2. With increasing fractionation, the progressive rise in the H_2O content of the melt causes X_{CO2} to steadily decrease, reaching ~65 wt% (40 mol%) at 0.5 wt% MgO (Fig. 5a). This decrease in the proportion of CO_2 in the fluid causes the CO_2 solubility predicted by MELTS model B (black dotted line, Fig. 3c) to decrease more rapidly than the model for pure CO_2 solubility. MELTS model B tracking mixed volatile solubility during fractional crystallization effectively brackets the upper limit of the majority of melt inclusion data, providing strong evidence that melts were vapour-saturated at depth, and that the solubility model MagmaSat used in Rhyolite-MELTS is effectively capturing changes in volatile solubility during fractional crystallization.

A significant proportion of the total amount of CO_2 in the system is lost to the vapour phase during fractional crystallization, partially because X_{CO2}>65 wt% across most of the fractionation interval, and because there was so little CO_2 in the system to start with (~385 ppm at 6.7 wt% MgO). For example, fractionation of just 0.02 wt% fluid with X_{CO2}=80 wt% removes 160 ppm of CO_2 from the system. In contrast, the higher initial mass of H_2O in the system combined with high X_{CO2} ratios mean that very little H_2O is lost to the fluid; in the example above only 40 ppm of H_2O is lost to the vapour compared to 160 ppm of CO_2. Notably, this is only ~1% of the initial amount of H_2O in the system, which is well within analytical error of SIMS measurements (Fig. 5b). Thus, the trajectory of melt H_2O during extensive fractional crystallization at shallow crustal pressures in the presence of an exsolved H_2O-CO_2 fluid is very similar to models of H_2O enrichment assuming no volatile loss. Minimal H_2O-loss to the exsolving fluid accounts for the high H_2O contents of the dacitic melts erupted at F17. We caution that the apparent incompatible behavior of H_2O should not be interpreted as evidence for "H_2O-undersaturation"; it may simply indicate that the magma was saturated in a mixed fluid that was relatively H_2O-poor.

While the upper limit of melt inclusion volatile contents follow MELTS model B, a number of melt inclusions plot to lower CO_2 and H_2O concentrations. The cause of this spread is best evaluated using plots of H_2O vs. CO_2, with degassing paths for specific melt inclusions overlain (calculated using the solubility model MagmaSat implemented in VESIcal; Ghiorso and Gualda, 2015; Iacovino et al., 2021; Fig. 6). Some samples (e.g., F10; Fig. 6b) show tightly clustered volatile contents, which plot very close to fractional crystallization trends (Fig. 3c-d). Others (e.g. F13-react, Fig. 6a) show considerable spread to lower CO_2 contents, approximately following the trajectory of modelled degassing paths. This indicates that many melt inclusions were formed or sealed during ascent, trapping a progressively degassing magma. Horizontal spread to variable H_2O contents may reflect diffusive re-equilibration of melt inclusions with degassing carrier melts, or crystals being entrained into melts with higher H_2O than those they grew from (e.g., 6 plag-hosted MI from F17). F17 melt inclusions show the most scatter, which can be recreated by a combination of the trajectory shown by MELTS model B, degassing, and H^+ re-equilibrium (Fig. 6d). However, without measurements of D/H ratios in melt inclusions, the exact contribution of degassing, fractional crystallization, and re-equilibration of H_2O is difficult to determine. In general, we note that H^+ loss through plagioclase is likely slower than in olivine (Johnson and Rossman, 2013). Additionally, we observe that multiple melt inclusions hosted within single crystals erupted at F17 have a wide range of H_2O-CO_2 contents, and there is no relationship between H_2O contents and the position of the melt inclusion within the crystal, or the size of the inclusion (inconsistent with H-loss by diffusion, Supporting Fig. S13-15). The observed variability within individual crystals is more consistent with melt inclusions being trapped at various points along a degassing path. The influence of degassing is considered further in section 4.5.

4.3 Implications for Eruption Style Variations

The higher water contents of F17 melts relative to basaltic and basaltic-andesite melts (resulting from larger amounts of fractional crystallization) means that a significantly larger volume of volatiles is exsolved as these melts ascend to the surface (Fig. 7c). We demonstrate this by tracking the ascent of magma along a closed-system degassing path in alphaMELTS for MATLAB for a composition representative of the basaltic material erupted at the early fissures (MgO=4.3 wt%, SiO_2=50.8 wt%, H_2O=0.95 wt%) and a composition representative of the dacitic melt erupted at F17 (MgO=1 wt%, H_2O=1.78 wt%; Fig. 7). For both melt compositions, these models predict that the volume of exsolved volatiles relative to the total volume of the system (fluid+melt+crystals) is very low at 650 to 400 bars (Fig. 7a), and degassing only produces measurable changes in the dissolved concentration of CO_2 in the melt (Fig. 7b). This is also shown on the degassing paths in Fig. 6a-d. At

<300 bars for the dacitic melt, H_2O begins to exsolve in larger quantities, causing the volume of exsolved volatiles to increase rapidly with decreasing pressure. The onset of significant quantities of H_2O exsolution occurs at a pressure ~100-200 bars lower for basaltic melts compared to dacitic melt.

To compare these ascent paths, we divide the volume of volatiles exsolved during ascent of the dacite by the volume of volatiles exsolved during ascent of the basaltic (Fig. 7a). The higher initial H_2O content of the dacite, combined with the fact that H_2O begins to exsolve at higher pressures means that at ~200 bars, the volume of volatiles in the dacitic melt is nine times higher than in the basaltic melt (Fig. 7c). The larger volatile volume at depth, combined with higher melt viscosity, will promote bubble nucleation and coalescence, which is a key driver of Strombolian activity (Jaupart and Vergniolle, 1988). By the time these melts reach the surface, where almost all of the initial H_2O in both melts has exsolved, the volume of volatiles exsolved in the dacitic melt is approximately twice that for the rift-stored basalts.

Eruption style is also influenced by melt viscosity. First, we model changes in melt viscosity during fractional crystallization (Fig. 5c), and then assess changes in viscosity during ascent using the viscosity model of Giordano et al. (2008) (Fig. 7d). As viscosity is highly sensitive to melt H_2O content, we calculate viscosity for the major and volatile-element trajectories from MELTS Model B, using MELTS temperatures and temperatures from Helz and Thornber (1987). Because Model B is a relatively poor fit to major element data at <4 wt% MgO, we also calculate the viscosity for the best fit to measured major and volatile element data (see Supporting Fig. S11) using the MgO geothermometer of Helz and Thornber, (1987) for melt temperature, and H_2O contents from a best fit to MELTS model B. The two viscosity models using Helz and Thornber (1987) are very similar, predicting a rapid increase in melt viscosity below 4 wt% MgO (Fig. 5b) as a result of SiO_2 enrichment in the melt following the onset of Fe-Ti oxide fractionation (Fig. 2a) and a steady decline in the temperature of the melt. The model using MELTS temperatures is similar until ~2 wt% MgO, after which it rises to higher values because MELTS predicts significantly lower temperatures than Helz and Thornber (1987).

Prior to the onset of degassing upon ascent, the dacitic melt is ~10-20 times more viscous than the basaltic melt (Fig. 7d). During ascent along a closed-system degassing path, the discrepancies in viscosity between the basaltic and dacitic melt are enhanced, so at the surface, the dacitic melt is 70-130 times more viscous (Fig. 7d, Soldati and Dingwell, 2021). The relative viscosities calculated in our models are very similar to viscosities obtained from direct measurements of 2018 lavas at atmospheric pressure (yellow and blue stars on Fig. 7d, Soldati and Dingwell, 2021) particularly when the Helz and Thornber, (1987) MgO thermometer is used for both comparisons. The increasing contrast in viscosity between the basalt and dacite during ascent to the surface results from the fact that the dacitic melt has more H_2O to lose (which drives a rapid increase in viscosity). It is also worth noting that these calculations only track the viscosity of the melt phase. While the proportion of crystals relative to melt is similar for F17 vs. early phase 1 lavas (~39% vs. 42%; Gansecki et al., 2019), F17 samples have completely different crystal shapes, with a larger number of smaller, elongated plagioclase crystals which may further amplify these differences in viscosity (see BSE images in Supplement Dataset S3, p78-80 vs. p82-84). The larger volume of bubbles in F17 melts will also affect viscosity, although this is difficult to quantify because it depends greatly on the amount of shear rate and strain of bubbles (Llewellin et al., 2002; Manga and Loewenberg, 2001).

It is well recognised that differences between Hawaiian style lava fountaining (exhibited weakly by the early fissures) and Strombolian activity (exhibited strongly by the F17 andesite) are controlled by magma rise speed, viscosity, and volatile content (Houghton et al., 2016; Houghton and

Gonnermann, 2008; Wilson and Head, 1981). Strombolian eruptions occur when bubbles can coalesce and rise faster than the surrounding melt, resulting in the bursting of large bubbles at the surface along with relatively minimal volumes of melt (see Supporting Video 1 and 2, Wilson and Head, 1981). Separated two phase flow is promoted at higher gas/magma ratios and for higher melt viscosities, which tends to reduce magma rise rates (Gonnermann and Manga, 2013). The 10-100 higher viscosities of F17 melts compared to more primitive basaltic melts at <300 bars (Fig. 7d), combined with the higher exsolved volatile fraction (Fig. 7c), mean that melt rise speeds would have been significantly slower for a given conduit width and pressure gradient, favouring bubble rise and coalescence (e.g., Parfitt and Wilson, 1995). Thus, the high explosivity observed at F17 is likely a direct consequence of extensive fractional crystallization driving up melt viscosity and H_2O contents, causing a larger volume of bubbles to exsolve (and coalescence) at greater depths in the conduit at a deeper depth, along with likely feedbacks between a higher viscosity and lower ascent rates in the dacitic melt (further favouring bubble coalescence).

4.4 Identifying Parental Magmas

Major and volatile element systematics indicate that melts erupted in the first two weeks of the 2018 eruption underwent extensive (and variable amounts) of fractional crystallization during rift-zone storage. However, using major elements systematics alone it is difficult to determine whether these melts were derived from fractionation of a single parent magma, or a number of different magma bodies, because the major element contents of different Kīlauea eruptions are relatively similar at a given MgO content (Helz and Wright, 1992). In contrast, through time, Kīlauea eruptions show clear variations in incompatible trace element ratios such as Nb/Y, La/Yb, and Zr/Y (Fig. 4b), interpreted to represent heterogeneity in the Hawaiian mantle plume, as well as variations in the degree of mantle melting (Pietruszka and Garcia, 1999a, 1999b). It is probable that the parent magma(s) for the variably-evolved melts erupted in 2018 were intruded into the rift zone and erupted at the surface during a previous eruptive episode (the most recent eruptive events occurred in 1790, 1823, 1840, 1955 and 1960 A.D). The 1790 and early 1955 fissures are of particular interest, because these fissures were located in the same area of the LERZ as the 2018 eruption (Fig. 1c; Helz, 2008; Moore, 1992; Wright and Fiske, 1971). Similarly, the 1960 eruption occurred a short distance downrift, so presumably its magma supply passed through the section of the rift zone were the 2018 eruption occurred. Here, we use trace element ratios to determine the composition of historic eruptions on the LERZ and compare these to our measurements from 2018 eruptive products to deduce the most probable parent magma(s).

Unlike previous work using trace elements to track magma batches at Kīlauea in lavas which have undergone mostly olivine-saturation (Pietruszka and Garcia, 1999b; Wieser et al., 2019), the melts analysed here have experienced fractionation of a number of phases (olivine, clinopyroxene, orthopyroxene, plagioclase, ±ilmenite, magnetite, and apatite). The presence of these other phases in addition to olivine provides a potential mechanism for these trace element ratios to be fractionated during crystallization, which might obscure attempts to compare rift-stored melt compositions to magma batches defined by analyses in the literature of mostly olivine-saturated samples from previous LERZ eruptions and Kīlauea's summit. To assess which element ratios are least fractionated by extensive crystallization at Kīlauea, we use the trace element systematics of glasses from drill cores taken through the Kīlauea Iki lava lake (Greaney et al., 2017). This lava lake experienced extensive fractionation of a single magma batch across a range of MgO contents very similar to the lavas examined here, with a very similar mineral assemblage (Helz, 1980; Helz and Thornber, 1987). Thus, evaluation of changes in trace element contents with decreasing MgO in these lava lake samples providing a unique opportunity to establish whether trace element ratios

are fractionated across this differentiation interval. Between 6 and ~0 wt% MgO, Kīlauea Iki matrix glass Nb, Yb and Y all increase by a factor of 2-3, while La and Zr behave more incompatibly; increasing by a factor of 3-4 times (Supporting Fig. S16). This causes the Nb/Y ratio to remain almost constant during extensive fractionation, while La/Yb increases slightly (~20%), and Zr/Y more than doubles (Supporting Fig. S17). Pietruszka et al., (2021) also demonstrate that Nb/Y is resistant to fractionation using available partitioning data for relevant phases. In addition to being the least fractionated ratio, it is also advantageous to use Nb/Y for comparisons because it is the only trace element ratio which has been reported by a number of different studies investigating historic lavas on the LERZ (because both Nb and Y can be measured accurately and precisely by XRF, unlike La and Yb).

Previous work has shown that Nb/Y ratios in historic summit and rift eruptions follow a prominent trough-peak-trough shape between 1800 to present (Garcia et al., 2021; Marske, 2010; Pietruszka and Garcia, 1999b, 1999a). The highest Nb/Y ratios are observed in lavas from the mid 1900s, declining towards the values measured during the final stages of the Pu‘u‘ō‘ō eruption (Fig. 4b; Gansecki et al., 2019). Nb/Y ratios from whole rock analyses of previous LERZ eruptions follow a similar trend to summit eruptions (Helz and Wright, 1992; Marske, 2010; Norman, 2005). Matrix glasses erupted in Early Phase 1 in 2018 have much more similar Nb/Y ratios to the 1955-1960 eruptions than melts erupted in the period between 1790-1840 AD (characterized by lower Nb/Y ratios; ~0.5-0.6, see also Pietruszka et al., 2021). This indicates that melts erupted in 1955 or 1960 are a more probable parent than those erupted in 1790 and 1840.

Two main phases of the 1955 eruption have been identified, with an early phase (1955E) thought to tap more MgO-poor magmas already present within the rift zone (5-5.7 wt % $MgO_{Whole\text{-}rock}$), while later phase (1995L) tapped more MgO-rich magmas (6.2-6.8 wt% $MgO_{Whole\text{-}rock}$) interpreted to reflect mixing of the 1955E lava with a more MgO-rich, summit-derived component (Helz and Wright, 1992). This is analogous to the temporal evolution from MgO-poor to MgO-rich observed in the 2018 eruption. Using the analyses of Marske (2010), along with additional analyses of 1955 lavas from Helz and Wright, (1992) and Norman, (2005), we show that the mean and range of Nb/Y ratios in lavas erupted in the early and late phase of 1955 are a good match to the matrix glass compositions erupted in Early Phase 1 in 2018 (Fig. 4a). Using Nb/Y ratios alone, it is not possible to definitively distinguish between the 1955E, 1955L and 1960 lavas, but it is notable that the 1955E vents are geographically extremely close to the 2018 vents (Fig. 1c).

Whole-rock Nb/Y ratios (pink dots on Fig. 4a, Pietruszka et al., 2021) of lavas erupted in the first 20 days of the 2018 eruption form a mixing trend between the “1955-1960 like” Nb/Y ratios exhibited by Early Phase 1 lavas, and the Nb/Y ratios measured in Phase 3. This trend is also seen in our matrix glass analyses of F13-react and F20. These mixing trends indicate that LERZ-stored melts were progressively flushed out by the more MgO-rich, lower Nb/Y component supplying phase 3 (Gansecki et al., 2019). Interestingly, while some of the more MgO-rich samples erupted at F17 (WR MgO=3-4 wt%, Gansecki et al., 2019; Pietruszka et al., 2021) show evidence for mixing with the lower Nb/Y component from Phase 3 (glass MgO=~0.5 wt%, WR MgO=2.3-2.6 wt%, Supporting Fig. S18), our sample has glass Nb/Y ratios which entirely overlap with these Early Phase 1 glasses (Fig. 4a). This overlap indicates that melts erupted in Early Phase 1 and at F17 were likely derived from a common parent magma, and that our F17 sample experienced minimal mixing with magma erupted in Phase 3. Thus, it seems likely that the initial activity at F17 was triggered by an increase in overpressure, change in crustal stress, or thermal rejuvenation resulting from the intrusion of a dike containing Phase 3 magma into this section of the rift zone, rather than as a direct consequence of mixing between different magma compositions. Subsequent mixing of magmas indicated by whole-

rock Nb/Y data from Gansecki et al., (2019) and Pietruszka et al., (2021; Supporting Fig. S18) likely helped to liberate more of this stored material, fuelling the large lava flows with more MgO-rich compositions that erupted from F17 until May 25th (not sampled in this study).

Melt inclusion Nb/Y ratios in plagioclase crystals show no correlation with the anorthite (An) content of the host (Fig. 4c), which is consistent with a common parental magma for all rift-stored melts. Similarly, melt inclusion Nb/Y ratios in olivine, clinopyroxene and orthopyroxene from early fissures show no correlation with host Mg# [Mg/(Mg+Fe) atomic; Fig. 4d)], and are clearly distinct from the significantly lower Nb/Y ratios in matrix glasses and the majority of melt inclusions in Phase 3. This indicates that very few inclusions trapped melts that had undergone significant mixing with Phase 3 melts. Interestingly, 3 plagioclase-hosted melt inclusions from early F8, F5 and F20 plot with F17 melt inclusions in Nb/Y-An space, and 6 inclusions from F17 have higher MgO contents and major element contents indicating post-entrapment cooling. This supports the idea that more MgO-poor pockets of melt exist in close proximity with more MgO-rich bodies in the rift zone magma body, in order for more MgO-rich fissures to scavenge more An-poor crystals, and for more MgO-poor fissures to scavenge more An-rich crystals. The five olivine-hosted melt inclusions erupted on May 28th in Phase 3 (F8) with higher Nb/Y ratios (~0.7; Fig. 4d) are hosted in olivines with some of the lowest forsterite contents of phase 3, and have melt inclusion TiO_2 contents overlapping with Early Phase 1 melt inclusions and glasses (Supporting Fig. S19). This indicates that they may have also grown from rift-stored melts with higher Nb/Y ratios, and these crystals were recycled into the lower Nb/Y Phase 3 melts.

Overall, melt inclusion Nb/Y ratios indicate that melt inclusions erupted in the first 2 weeks of 2018 likely crystallized from a single parent magma body (or a series of magma bodies with similar parental magmas), and that very few melt inclusions crystallized following mixing between rift-stored and Phase 3 melts (although crystal recycling between different stored magma batches did occur).

4.5 Pre-eruptive magma storage depths

Melt inclusion H_2O and CO_2 contents provide further constraints on the nature of magma storage within the LERZ. The increase in H_2O and decrease in CO_2 with decreasing MgO content (Fig. 3c-d) provide strong evidence that melts were volatile-saturated throughout the fractionation interval considered here. Thus, estimates of the melt inclusion temperature, major elements, H_2O and CO_2 contents at the time of entrapment may be used to calculate the pressure at which those dissolved volatile contents would be saturated, and, by extension, the pressure at which the melt inclusion was trapped within its host crystal. This is termed the “saturation pressure”, or “entrapment pressure”. By estimating the crustal density profile, these saturation pressures can be converted into depths within the volcanic edifice.

As discussed in section 4.2, H_2O-CO_2 systematics indicate that a number of melt inclusions were likely trapped during ascent, after degassing had begun. While these still yield useful saturation pressures (indicating the depths at which inclusions are forming on the way to the surface), we also filter the dataset to only consider melt inclusions trapped from magmas prior to the onset of degassing on ascent to identify magma storage reservoirs. To remove melt inclusions trapped during degassing, we exclude inclusions with CO_2 contents lying more than 30% below the CO_2 content predicted by MELTS model B at the MgO content of each melt inclusion. To remove inclusions which have undergone H_2O degassing or diffusive re-equilibration, we filter inclusions more than ±30% from MELTS model B. An example of this filtering process is shown in Fig. 6d-f for F17 melt

inclusions. Melt inclusions meeting both criteria are marked with red crosses (see also Supporting Fig. S20).

We use the solubility model MagmaSat (Ghiorso and Gualda, 2015) implemented in the Python3 tool VESIcal (v.0.01; Iacovino et al., 2021) to calculate entrapment pressures from PEC-corrected major element, H_2O, and CO_2 contents of each melt inclusion, and a temperature estimated using the Helz and Thornber (1987) MgO thermometer. We choose MagmaSat because this model provides the best fit of available models to experimental data with basaltic to dacitic compositions, as a result of its thermodynamic nature and extensive calibration dataset (P. Wieser et al., 2021). Additionally, use of this model provides consistency with our models of volatile solubility during fractionation and ascent, as MagmaSat is the solubility model used in Rhyolite-MELTS v.1.2.0.

Filtered early phase 1 melt inclusions show a distinct clustering of saturation pressures at ~0.48-0.8 kbar, with 4 inclusions spanning pressures up to 1.15 kbars (Fig. 8a). Filtered F17 melt inclusions show a remarkable overlap with Early Phase 1, mostly spanning 0.55 – 0.8 kbar, with 2 higher pressure inclusions (Fig. 8b). Only two melt inclusions from F13-react and five from F20 pass our filters (Fig6a, c, Fig. 8c-d, Supporting Fig. S20), but these also yield very similar pressure distributions. Unfiltered data for all samples stretches to significantly lower pressures, indicating that a number of melt inclusions were likely trapped during ascent (fig. 8e-h). It is worth noting that melt inclusions from F13-react and F20 samples show clusters at 0.01-0.03 wt% CO_2, which could indicate that a large number of inclusions were trapped during degassing, or that these fissures were tapping a slightly shallower magma reservoir.

Using a crustal density of ρ=2600 kg/m^3 based on the relationship between drill depth and pressure presented from borehole drilling results at Puna Geothermal Venture from Teplow et al. (2009), melt inclusion saturation pressures can be converted into magma storage depths. Filtered melt inclusions cluster between ~2-3 km (Fig. 8), which aligns remarkably well with the depth of a V_p/V_s anomaly imaged in this area centred at 2 km depth between Pu‘uhonua‘ula and Pu‘ulena Crater (Fig. 1b) with a vertical extent of 1.5 km (Cooper and Dustman, 1995). The lateral dimensions of this body (2.5 km parallel to the rift zone, 2 km perpendicular to the rift zone) means that it directly underlies the fissures erupted in the first two weeks of the 2018 eruption. Thus, it is highly probable that the magma body being tapped by the 2018 eruption is the source of this seismic anomaly. Similarly, F17 saturation pressures align remarkably well with the depth at which an even more silicic dacitic magma was drilled at the PGV injection well KS-13 in 2005 (depth of 2488m, ~650 bars pressure, yellow star on Fig. 8).

4.6 Temporal evolution of Kīlauea’s LERZ

We present a schematic model summarizing the evolution of Kīlauea’s LERZ, based on our findings and previous work on historic lava samples (Fig. 9). The early fissures of the 1955 eruption, which are located very close to the 2018 eruption site (Fig. 1c), tapped melts with whole-rock contents of ~ 5-5.7 wt% MgO. These melts were likely resident in the rift zone since at least since 1924 (when a dike swarm propagated past the 2018 eruption site into Kapoho) or 1790 (the last eruption where magma breached the surface in this section of the LERZ; Fig. 1c). Alternatively, ^{230}Th-^{226}Ra dating of 1955E lavas suggests that clinopyroxenes and plagioclases were resident for at least 550 years prior to eruption. The later phases of the 1955 eruption focused at fissures uprift of the 2018 eruption site tapped more MgO-rich magmas (6.2-6.8 wt% $MgO_{Whole\text{-}rock}$) which have been interpreted to reflect renewed supply from the summit reservoir (Helz and Wright, 1992; Fig. 9a). This resupply may have propagated downrift, helping to replenish reservoirs depleted during the early phases of the 1955 eruption. In 1960, activity commenced downrift of the 1955E fissures, first trapping stored magma

with chemical similarities to the 1955 lavas (6.1-6.6 wt% $MgO_{Whole\text{-}rock}$), followed by the appearance of progressively higher MgO contents associated with supply of material from Kīlauea's summit reservoir (7-13 wt% $MgO_{Whole\text{-}rock}$, Russell and Stanley, 1990). As in the later phases of the 1955 eruption, the 1960 summit resupply may also have replenished the larger reservoir complex residing beneath the 2018 eruption site (as the 1960 magmas are very similar in terms of Nb/Y and major elements; Russell and Stanley, 1990, Fig. 9b). This pulse of activity in 1955-1960 left substantial amounts of magma at depth, which continued to cool and fractionate over the next 60 years as activity shifted to Kīlauea's summit, South West Rift Zone and Middle East Rift Zone. In 2005, a dacitic pocket of magma was encountered during geothermal drilling (Fig. 9c).

The propagation of a dike downrift from Pu'u'ō'ō on April 30th, 2018, disturbed these rift-stored melts, with magma erupting at the surface beginning on May 3rd (Fig. 9d). After a short pause after May 9th, erupted melt compositions between the 12-18th of May begin to show mixing between LERZ-stored and dike-supplied melts (e.g. in matrix glass Nb/Y ratios, Fig. 4a, Gansecki et al., 2019, Supporting Fig. S18), although erupted crystals are still dominated by geochemical signatures indicative of the LERZ-stored component (Fig. 4c-d). Dacitic melts also began erupting at F17, and Fissure 13 shows mixing between these dacitic melts and the more MgO-rich LERZ-stored component. By the time activity focused at Ahu'ailā'au (F8) on May 28th, almost all LERZ-stored crystals (and melts) had been flushed out by dike stored material (Fig. 9e, Fig. 4d, Supporting Fig. S19).

It is noteworthy that Early Phase 1 lavas have similar MgO contents of early 1955 lavas, so if these are the parent, the portion of the reservoir tapped by Early Phase 1 fissures must have been sufficiently thermally buffered that minimal fractionation took place over ~60 years. Relatively slow cooling rates within a thermally buffered magma body are consistent with ~500 year residence times inferred for the early 1955 lavas by Cooper et al. (2001). Alternatively, the 1955E reservoir may have been topped up by more MgO-rich magma in the later phases of the 1955 eruption or the 1960 eruption (Fig. 9b).

The larger amount of fractional crystallization experienced by F17 melts erupting on May 14th and the dacitic magma encountered during drilling in 2005 compared to melts erupted between May 3-9th is intriguing. The similarity of melt inclusion saturation pressures and drilling depths between all three samples, and similarity of Nb/Y ratios between Early Phase 1 and F17 from these samples indicate that the melts supplying all three bodies had a similar parent magma, and were stored at a similar depth. We suggest that the F17 dacitic melt may formed on the periphery of the larger magma body located in this region, allowing more cooling to occur in a specific amount of time (Fig. 9d). This interpretation is supported by the fact that F17 is offset ~220 m NE from the trend defined by other fissures. Pockets of dacitic melt may also have formed within regions of enhanced hydrothermal cooling. Deconvolving the nature of the evolution of this complex LERZ magma body in space and time will likely require detailed thermal modelling, and isotopic data to provide a more precise way to identify different magma batches with more resolution than can be achieved using incompatible trace element ratios.

5. Global occurrence of more silicic melts in basalt-dominated volcanic region

Analyses of erupted matrix glasses and melt inclusions from the 2018 eruption demonstrate that extensive crystallization of an ocean island basalt causes substantial enrichment in incompatible volatile and trace element species (Cl, F, H_2O). In particular, the increase in melt H_2O contents

combined with a rapid increase in melt viscosity following Fe-Ti oxide fractionation means that these silicic magmas have the potential to display more explosive eruption styles relative to the more typical Hawaiian style exhibited by basaltic to basaltic-andesite magmas.

The eruption of dacitic melt in 2018 at Kīlauea provides support to the growing volume of literature indicating that andesitic-rhyolitic magmas are more common than we thought in predominantly basalt-dominated volcanic regions. For example, Stock et al. (2020) report low An plagioclase crystals (down to An_{48}) in basaltic lava and reticulite dominated by a higher An plagioclase population (An_{78-82}) from the 2015 eruption of Volcan Wolf in the Galapagos Archipelego. They also identify low An plagioclase crystals in gabbroic nodules from the 1968 Fernandina eruption. Fractionation models indicate that these plagioclase crystals must have grown from basaltic trachy-andesite and trachy-andesitic melts. Additionally, resorbed quartz has been identified in tephra from the 2015 eruption of Wolf. This indicates that the subvolcanic plumbing system at these two volcanoes which erupt monotonous basaltic compositions must contain highly fractionated, silicic melts at depth not yet observed at the surface.

Rhyolites comprise approximately 10% of erupted lavas in Iceland (Jónasson, 2007), and have been noted in a variety of settings among mid-oceanic ridges (Wanless et al., 2010). While the continuum of melt inclusion major element contents from basalt to dacite, and good fit of major, volatile and trace element contents to MELTS fractional crystallization models indicate that Kīlauea dacites result from extensive fractional crystallization, silicic magma occurrences in Iceland and MOR have been variably attributed to fractional crystallization, crystal-melt segregation, and partial melting of hydrothermally altered crust based on isotopic, volatile, major and trace element data (Elders et al., 2011; Geist et al., 2021; Masotta et al., 2018; Rooyakkers et al., 2021a; Wanless et al., 2010).

Interestingly, Rooyakkers et al. (2021b) highlight the fact that silicic magmas have been encountered 4 times in the last two decades years during borehole drilling: dacite at Kīlauea (Teplow et al., 2009), trachyte in Menegai, Kenya (Mbia et al., 2015), and rhyolite on two occasions at Krafla (Elders et al., 2011; Mortensen et al., 2010). While the Mengeai and Krafla drilling encounters were a little less surprising in terms of the composition encountered compared to Kīlauea (because rhyolitic and syenetic magmas are better represented in surface deposits at these locations), It is noteworthy that all of these encounters intercepted silicic magmas at very similar depths (2488 m at Kīlauea, ~2000 m in Kenya, 2571 m and 2104 m at Krafla), all in areas of active hydrothermal exploration. Although these silicic magmas may be generated by different mechanisms, all require high heat fluxes at shallow levels, either to melt/rejuvenate existing material, or to allow fractional crystallization to proceed without the magma simply freezing in the crust. At Kīlauea, this high heat flow likely results from the focus of repeated intrusion over hundreds of years in this particular section of the rift zone, perhaps resulting from a “jog” in the rift zone, with two offset branches creating a local extension stress field (Kenedi et al., 2010). This is somewhat analogous to the higher focusing of melt, and therefore higher occurrence of silicic magma in overlapping spreading centers of mid-oceanic ridges (Kent et al., 2000).

While 2018 marked the first documented occurrence of dacitic melt erupting at the surface, given that 70% of Kīlauea’s surface is <500 yrs old, and 90% is <1100 yrs old (Holcomb, 1987), these melts could erupt on a centurial-millenial basis, and still be absent in surface exposures. This is particularly true given that dacitic melts are most likely to form in parts of the volcano characterised by high intrusion rates, to maintain the high heat fluxes at shallow levels required for melts to fractionate to dacitic compositions without freezing in the crust. In turn, high intrusion rates mean these sites are most likely to be rapidly resurfaced by volcanic activity. For example, 75% of the surface of the

lower-east rift zone is <500 yrs old (Moore, 1992) . If magmas with silicic compositions were able to evade sampling at Kīlauea, one of the world's best-studied ocean island volcanoes, prior to drilling in 2005, it seems highly likely that these compositions are present at other ocean island volcanoes. Specifically, based on the need for high heat flow to generate silicic magma bodies, and the increasing number of drilling encounters, the anomalously hot areas of ocean islands are not only the most likely to contain more silicic melts at shallow depths, but will also be the preferred targets for hydrothermal exploration.

When the dacitic body was drilled at Kīlauea in 2005 at 2488 m depth, it was noted that the glass did not show vesiculation (Teplow et al 2009), leading to inferences that the magma was volatile-poor. Given that our melt inclusion measurements demonstrate that F17 melts were H_2O-rich, we instead hypothesize that the low vesicularity resulted from the fact that a relatively small mass of volatiles is exsolved during fractionation from a basalt to dacite (~0.04 wt%) at this depth, meaning there is limited potential for a large, gas-rich cap to develop on top of these bodies (Fig. 5a). Upon ascent, significant quantities of H_2O only begin to exsolve from a dacitic melt composition at ~300 bars. Thus, as long as the drilling fluid quenches these silicic melts at higher confining pressures, there would be limited potential for large amounts of volatile exsolution and catastrophic well blowout (Teplow et al., 2009). However, if allowed to rise to shallow levels prior to quenching, silicic melts could present a hazard to geothermal drilling in basalt-dominated settings.

In addition to being encountered during drilling, it appears that the eruption of silicic melts at the surface may be closely coupled to the injection of basaltic dikes into the region. At Kīlauea, based on the limited evidence for mixing between the dacite and the dike-supplied magma in the initial products of F17, we suggest that dike injection increased overpressure or changed the stress state in the magma body, causing the eruption. Similarly, Rooyakkers et al., (2021b) examine the rhyolitic magma producing the Víti maar at Krafla, Iceland, and conclude that these melts show very little textural or chemical evidence for mingling/mixing with the basaltic "trigger". This contrasts with explosive eruptions like Askja, 1875 which show clear evidence textural evidence for pre-eruptive magma mixing (Sparks et al., 1977). Clearly, the potential of silicic magma bodies to generate explosive eruptions should be considered during hazard assessments in a wide variety of ocean islands and other basalt-dominated settings (Rooyakkers et al., 2021b), both in terms of natural eruptions initiated by a dike, and drilling encounters.

6. Conclusions

Basaltic to andesitic magmas erupted during the first two weeks of the 2018 eruption (3rd – 16th May) were likely formed from variable amounts of crystallization of a magma body at ~2-3 km depth within the LERZ. The similarity in Nb/Y ratios in melt inclusions from these early eruptive fissures and a range of host crystal chemistry implies that crystallization proceeded from a single magma parent body (or a series of bodies with near-identical trace element chemistry). Comparison of Nb/Y ratios to historic LERZ lavas indicates that melts erupted in 1955-1960 are the most likely parent to the early 2018 lavas (see also Helz, 2008; Pietruszka et al., 2021; Teplow et al., 2009). Extensive crystallization of a section of this larger magma body (perhaps on the periphery or in a region with enhanced hydrothermal cooling) produced a dacitic melt composition highly enriched in incompatible elements such as Cl, F, Zr, and H_2O. Combined with an increase in magma viscosity with increasing SiO_2 content and dropping temperatures, this H_2O-enrichment accounts for the explosive strombolian behavior exhibited by the eruptive fissure tapping this melt (F17) without requiring external sources of volatiles such as groundwater. Although the high viscosities of these dacitic melts mean they are unlikely to erupt spontaneously, the 2018 eruption shows that they may be triggered

by the injection of basaltic intrusion. The volatile-rich nature of these bodies should also be considered when prospecting for geothermal wells; if the melt erupted at F17 had been drilled and allowed to depressurize to ~300 bars prior to quenching, large amounts of vesiculation may occur.

Figures

(see attached pdfs for higher resolution figs)

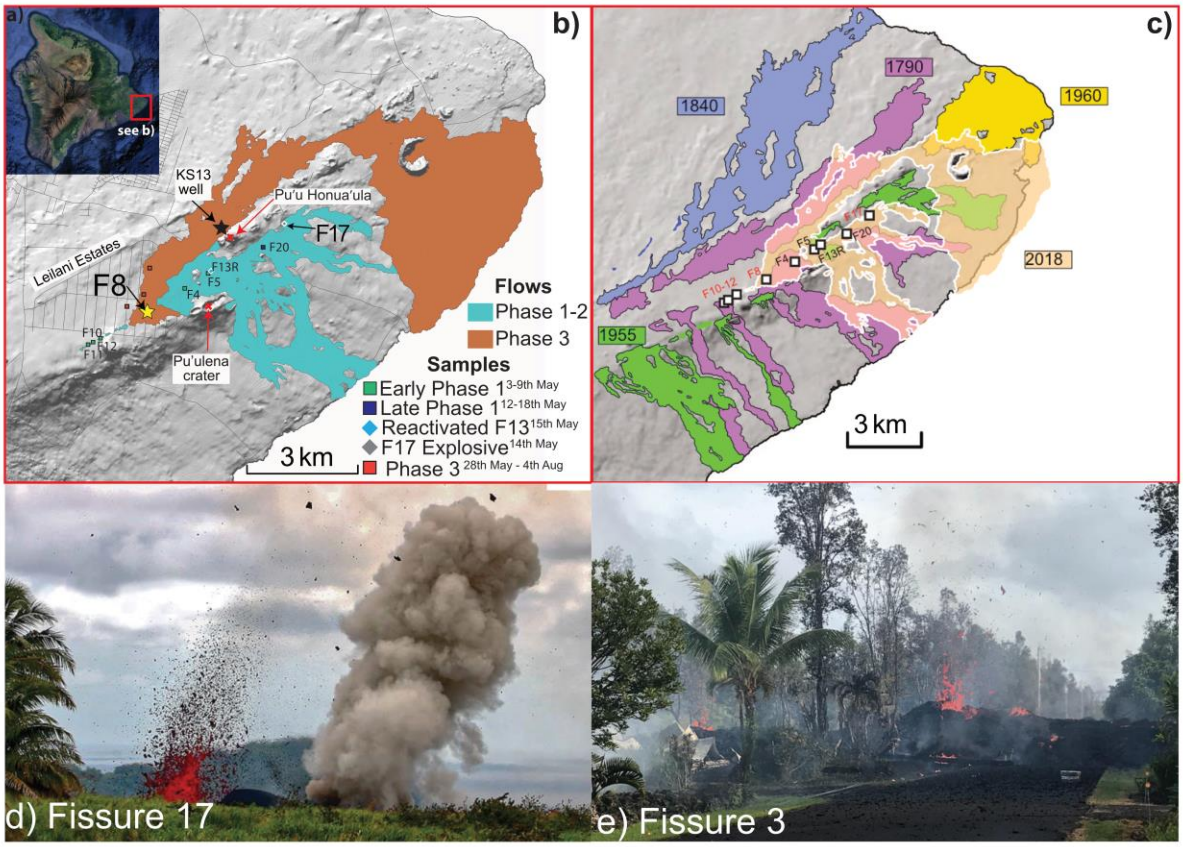

Figure 1 – a) Map of the island of Hawai'i, with the area inside the red box expanded in b). b) Hillshade map from DEM of the Lower East Rift Zone showing the fissures and lava flows produced during the 2018 eruption. Locations of samples analysed in this study are shown with colored symbols. Ahu'ailā'au (F8) is marked with a yellow star, and the location of borehole KS13 where a dacitic magma was drilled in 2005 is shown with a black star. Pu'uhonua'ula and Pu'ulena Crater are marked with red crosses (reference points for the position of the seismic anomaly). c) Map showing the location of previous eruptive episodes on the LERZ, with the 2018 flows overlain in pale pink. d) F17 showing the difference in eruption style between the basaltic-andesite eastern end (low fountaining and spattering, LHS), and the more silicic andesitic western end (strombolian explosions and gas jetting, RHS). e) Low spatter mounds produced during the first day of the eruption at F3. Photos in d and e) from USGS. Part b) was adapted from Patrick et al., (2019), and c) from Pietruszka et al., (2021), using geospatial data from Trusdell et al., 2006; Zoeller et al., 2020

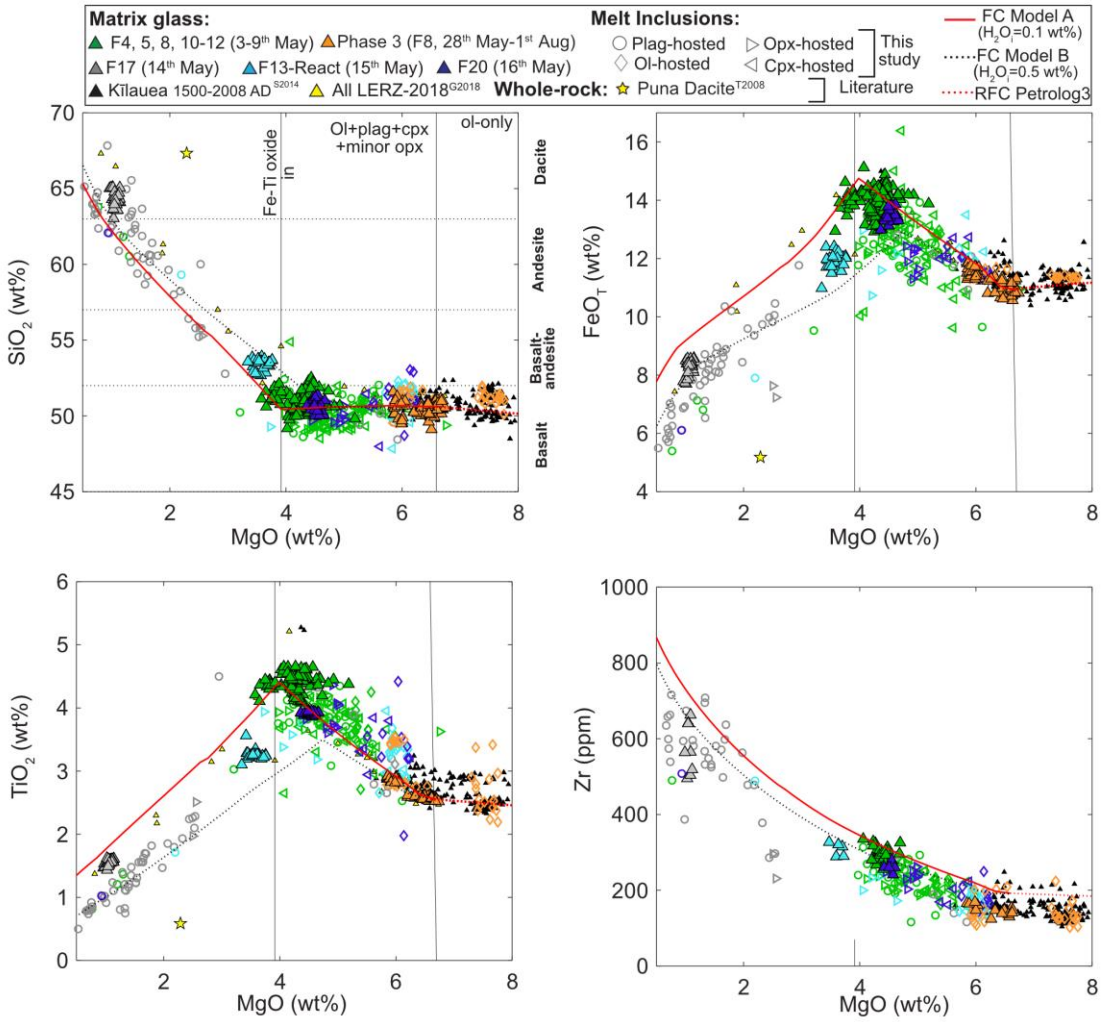

Figure 2- Major element systematics of matrix glasses and melt inclusions. The composition of olivine, clinopyroxene and 6 plagioclase melt inclusions are corrected for the effects of PEC. Literature data for matrix glasses erupted during the 2018 eruption (yellow triangles, Gansecki et al., 2019) and previous Kīlauea eruptions (black triangles, Sides et al., 2014a, 2014b; Wieser et al., 2019) are shown, along with the whole-rock composition of the dacitic magma drilled in 2005 (Teplow et al., 2009). Two fractional crystallization models run in alphaMELTS for MATLAB (Rhyolite-MELTS v1.2.0, Antoshechkina and Ghiorso, 2018; Ghiorso and Gualda, 2015; Gualda et al., 2012) are shown, with $Fe^{3+}/Fe_{T,\ initial}$=0.15 (unbuffered), P=650 bars. Model A uses an initial H2O content of 0.1 wt% (red line, best recreates the onset of Fe-Ti oxide saturation), while Model B uses a more realistic initial H_2O content of 0.5 wt% (black dashed line). As the rhyolite-MELTS model fails to recreate the olivine-only fractionation assemblage at >6.8 wt% (Wright and Fiske, 1971), the red dashed line shows a reverse fractionation crystallization (RFC) model run from the starting composition in Petrolog3.1.3 (Danyushevsky and Plechov, 2011). The fractionation trajectory for Zr is calculated assuming incompatible behavior.

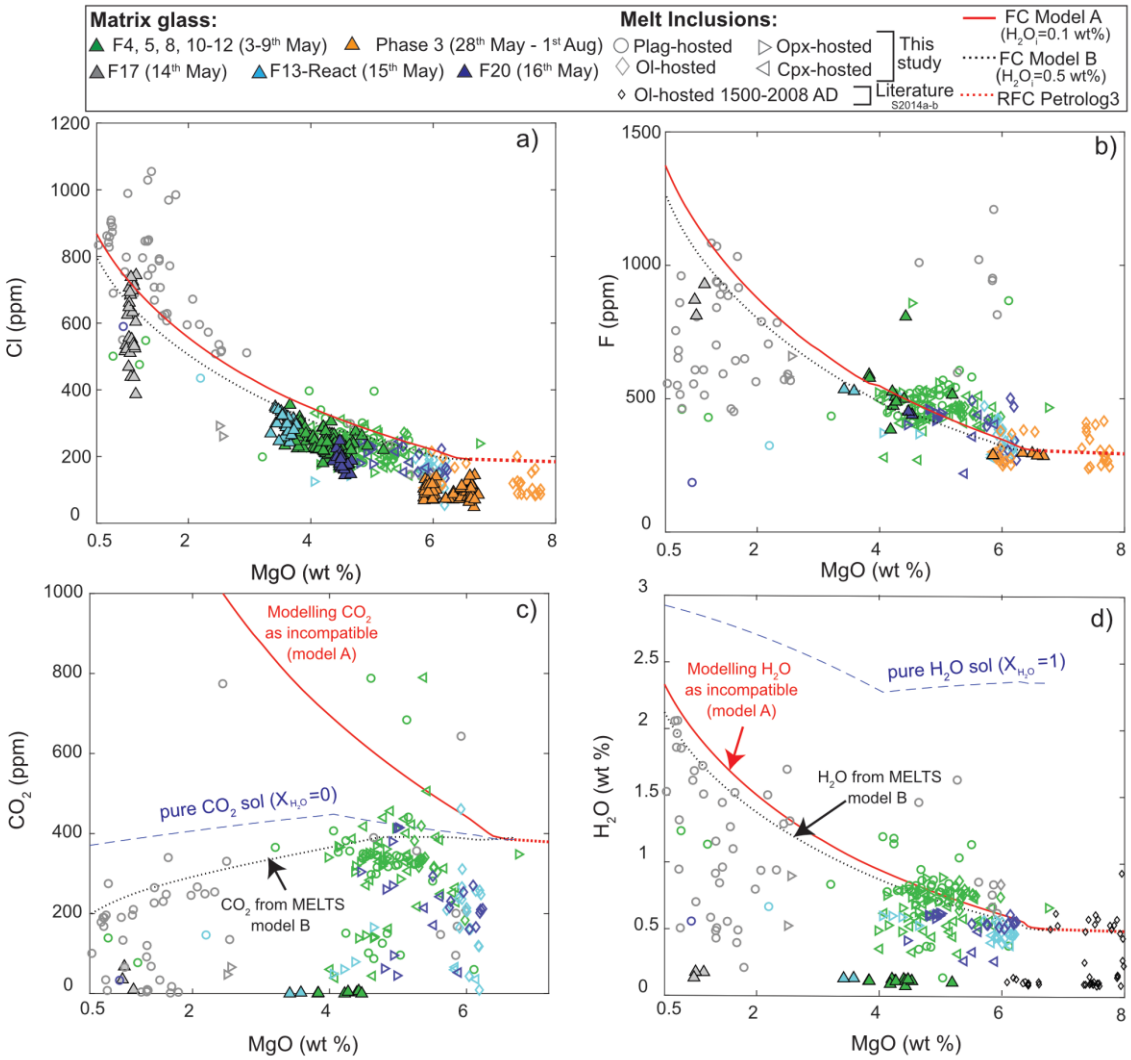

Figure 3– Volatile element systematics, with fractionation trajectories assuming perfect incompatibility for all elements from MELTS model A shown in red. Incompatible behavior is assumed for Cl and F in MELTS model B, while CO_2 and H_2O solubility in equilibrium with a mixed fluid are tracked in the solubility model MagmaSat integrated into MELTS (dashed black line). The dashed red section of the line shows reverse crystallization of olivine from the starting composition in Petrolog3. For Cl and F, models A and B produce very similar trajectories, as these models predict similar amounts of solid fractionated. The solubility of pure CO_2 and H_2O calculated using the MagmaSat solubility model (Ghiorso and Gualda, 2015) implemented in VESIcal (Iacovino et al., 2021) for a best-fit to the observed major element path (see Supporting Fig. S11) is shown with a blue dashed line.

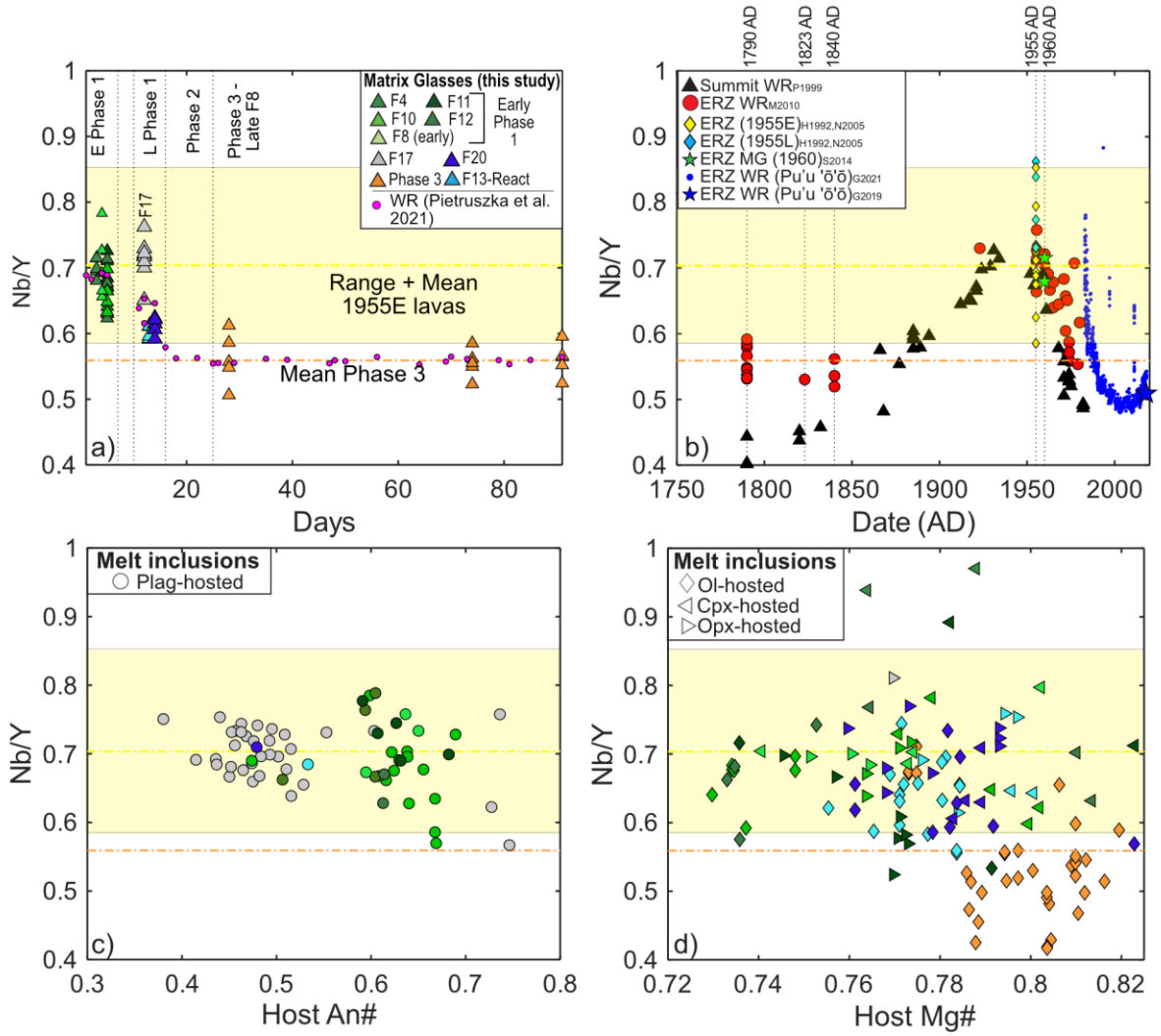

Figure 4– Ratios of incompatible trace elements in 2018 eruption products and previous LERZ eruptions. **a)** variations in Nb/Y in co-erupted matrix glasses (this study) with time throughout the eruption (May 3rd = Day 1). Whole-rock measurements from Pietruszka et al. (2021) are overlain. **b)** Compilation of Nb/Y ratios versus time for whole-rock measurements of summit lavas (black triangles, Pietruszka and Garcia, 1999), LERZ lavas from 1790, 1823, 1840, 1955, 1960 (red dots, Marske, 2010), early phases of the 1955 LERZ eruption (yellow colors), and later phases (cyan colors, Helz and Wright, 1992; Norman, 2005). Analyses of matrix glass from the 1960 Kapoho eruption from Sides et al., (2014b) and whole-rock measurements from Pu'u'ō'ō are also shown (Gansecki et al., 2019; Garcia et al., 2021). The mean composition of the early 1955 lavas and Phase 3 matrix glasses are shown with a yellow and orange dashed line on all plots, with the range for 1955 shown in light yellow. **c)** Nb/Y ratios in plagioclase-hosted melt inclusions vs. host anorthite content. **d)** Nb/Y ratios vs. host Mg# for olivine, orthopyroxene and clinopyroxene-hosted melt inclusions. Symbols in part c-d are colored by fissure as in part b.

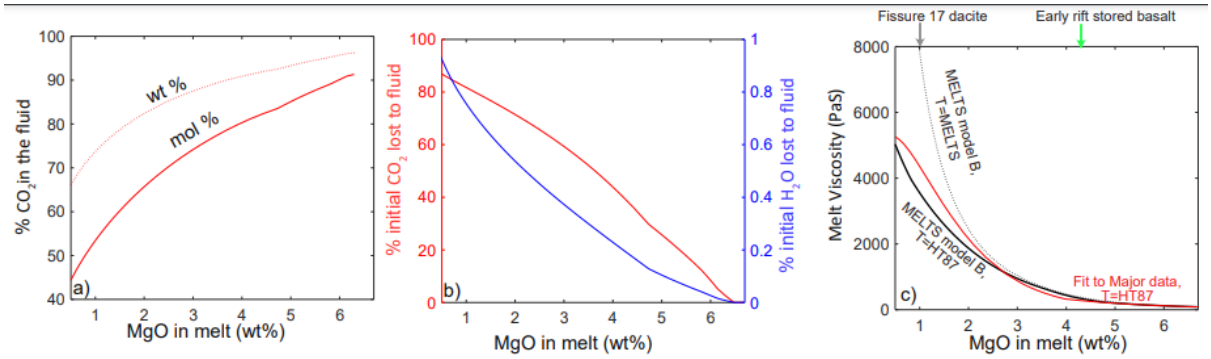

Figure 5- Volatile exsolution and changes in viscosity during fractional crystallization tracked in MELTS model B. **a)** % of CO_2 in the exsolved fluid (by wt% and mol%) decreases with progressive fractionation. **b)** % of the initial amount of CO_2 (red solid line) and H_2O (blue solid line) lost to the fluid phase during fractionation. **c)** Changes in viscosity during fractionation. The black dashed line shows viscosity from MELTS model B using Giordano et al., (2008) and the MELTS temperature, and the black solid line shows MELTS model B with temperatures calculated from the MELTS MgO content using the Helz and Thornber (1987) MgO thermometer. The red line shows the viscosity calculated using Giordano et al., (2008) for the best-fit model to measured major elements (Supporting Fig. S11), with temperatures calculated using Helz and Thornber (1987), and H_2O contents estimated for a parameterization of the relationship between H_2O and MgO shown as a red line in Fig. 3d.

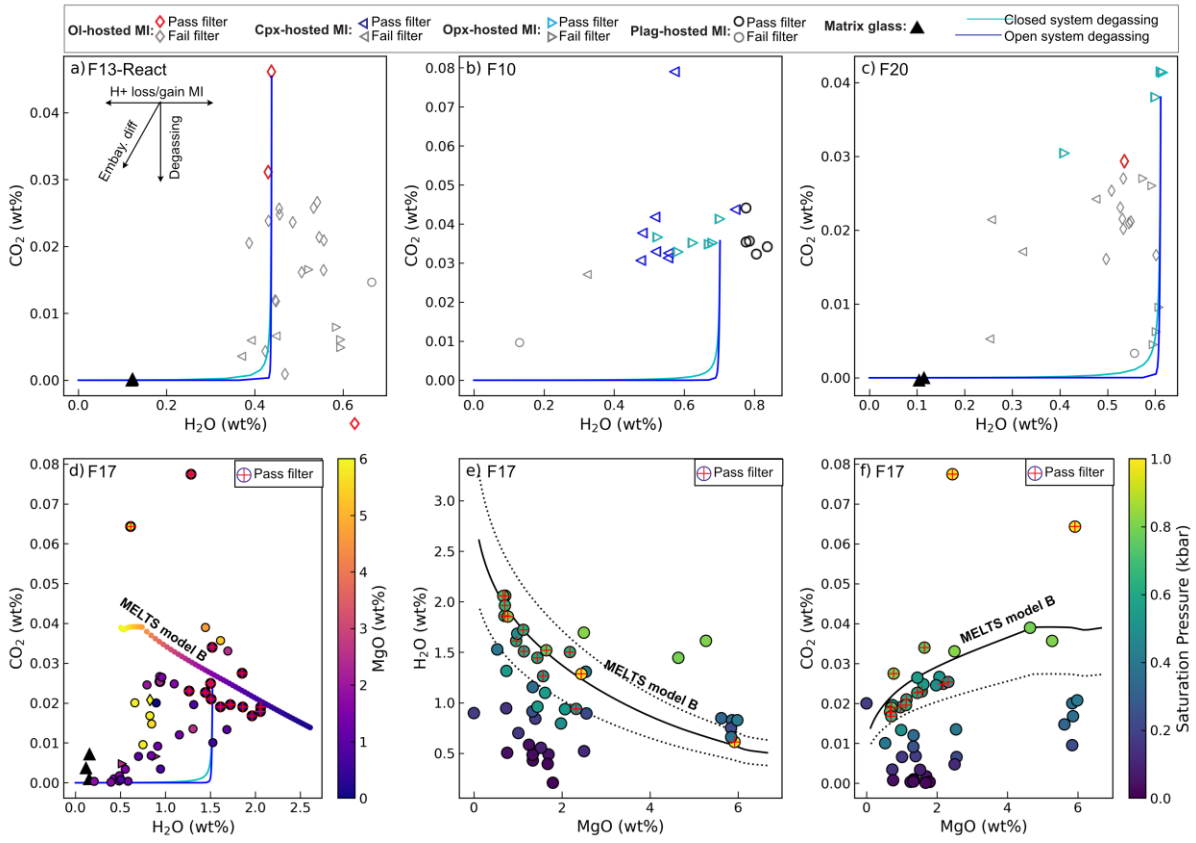

Fig. 6. a-c) Example degassing paths for three fissures, with open and closed system degassing paths calculated using MagmaSat (Ghiorso and Gualda, 2015) in VESIcal (Iacovino et al., 2021) for specific melt inclusions overlain. Vectors for different processes are shown in a). d) Degassing path for F17 with melt inclusions colored by their MgO content. The trajectories caused by degassing (blue and cyan lines) and fractional crystallization (yellow-purple line) are overlain. e-f) Example of the filtering process used to calculate saturation pressures for F17. Only melt inclusions with CO_2 contents less than 30% below the MELTS fractionation line (filtering out degassing), and only H_2O contents within +-30% are used (filtering out degassing and H+ re-equilibration to higher and lower values). Symbols are colored by their saturation pressure, and are marked with a red cross if they pass both filters.

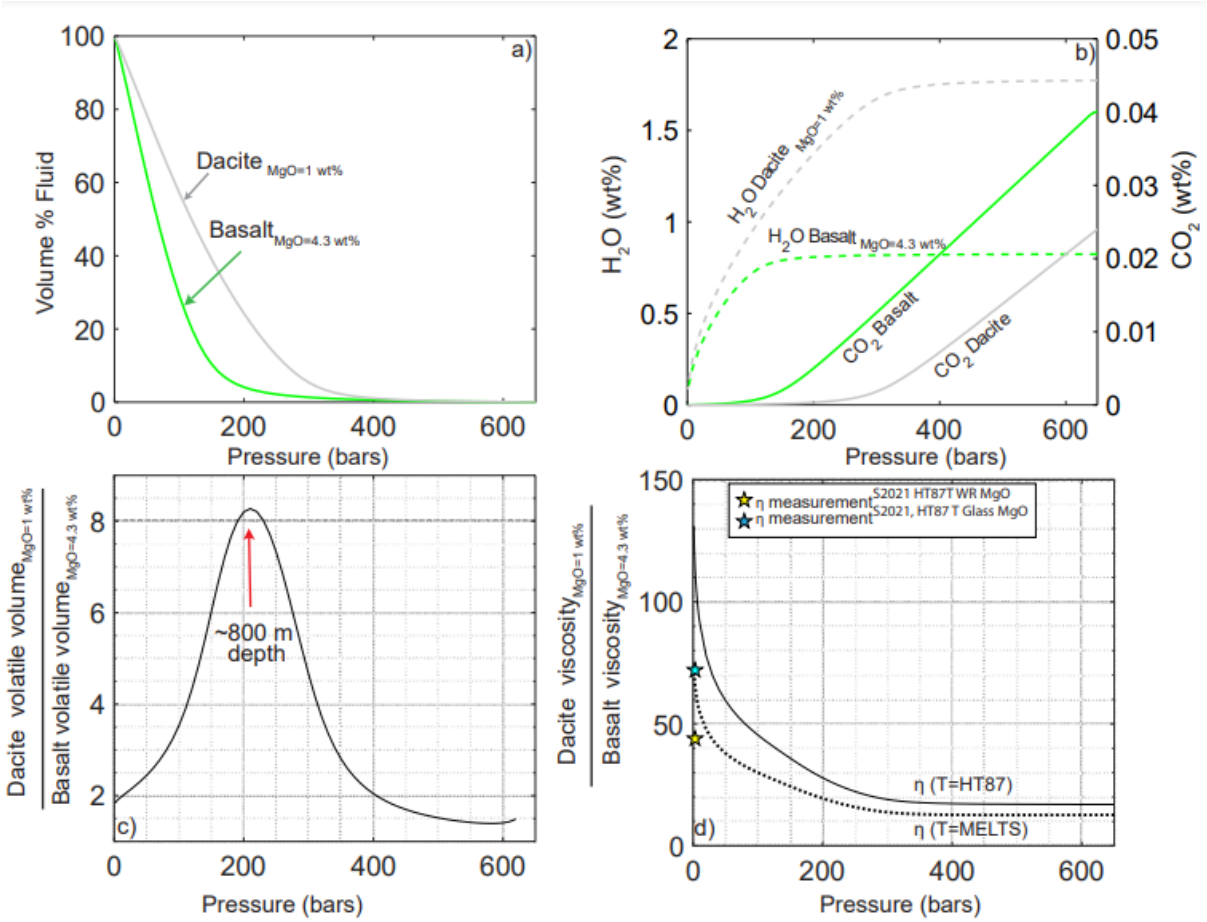

Figure 7. Volatile exsolution and changes in viscosity during ascent to the surface along a closed system degassing path for a basaltic andesite (BA) melt (~4.3 wt% MgO, average composition of Early Phase 1 matrix glasses), and a dacitic melt composition (MgO=1 wt%, average composition of F17 matrix glasses). **a)** Volume of the exsolved fluid phase relative to the total volume of the system for both melt compositions with decreasing pressure**. b)** Concentration of H_2O (LH axis, dashed lines), and CO_2 in the melt (RH- solid lines) during ascent. **c-d)** Comparison of the volume of volatiles and viscosity during ascent of the dacitic and basaltic andesite melt. **c).** The volume of exsolved volatiles is ~8-9 times higher for the dacite at ~200 bars (800 m depth), because of the higher H_2O content of this melt, and the earlier exsolution of H_2O from this melt relative to the basalt **(b).** Even at the surface, the volume of exsolved volatiles is ~2 times higher for the dacite. **d)** The viscosity of the dacite divided by the viscosity of the basalt at each point on the ascent path calculated using the Giordano et al., 2008 model. The dashed line shows viscosity using the temperature from MELTS,

and the solid line shows temperature calculated from the MELTS MgO content using Helz and Thornber (1987). The yellow star shows the viscosity ratio between the dacitic F17 lavas and the basaltic/basaltic-andesite Early phase 1 lavas reported by Soldati and Dingwell, (2021), using temperatures they calculate from whole-rock MgO contents using Helz and Thornber (1987). The cyan star uses their viscosity parameters (A, B, C) to calculate viscosity at the temperatures for the MgO contents considered here for the dacitic melt (1 wt% MgO) and basaltic melt (4.3 wt% MgO) using Helz and Thornber (1987). The lower MgO content of our F17 glass relative to their whole-rock measurement result in a lower temperature, so a higher viscosity.

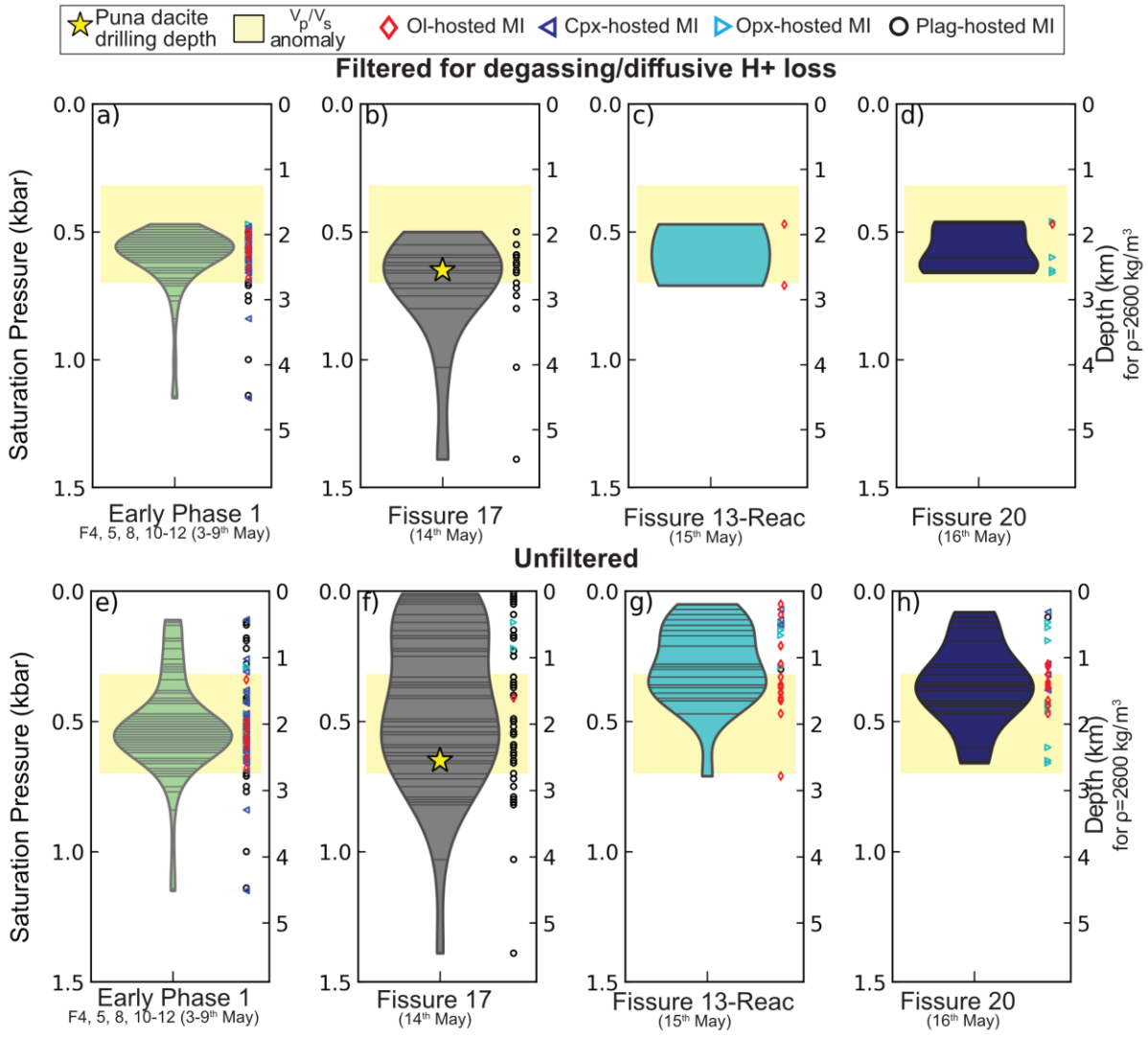

Figure 8. Magma storage depths for different early fissures from the 2018 eruption. A-h) Violin plots showing saturation pressures calculated using the solubility model MagmaSat (Ghiorso and Gualda, 2015) implemented through VESIcal (Iacovino et al. 2021). A-d) shows filtered melt inclusions (within ±30% of MELTS model B for H_2O, and -30% for CO_2, see Fig. 6e-f). e-h) shows all melt inclusions. Each grey line on the violin plot represents a melt inclusion, and the width of the "violin" represents the clustering of data at each pressure. On the RHS, the individual saturation depths for each inclusion are shown with symbol shapes and colors corresponding to the host phase. The depth at which the

dacitic magma was drilled at PGV is shown as a yellow star, and the depth of the low Vp/Vs region (low of Vp/Vs=1.66 vs. 1.78 background) imaged by Cooper and Dustman (1995) is shown in yellow.

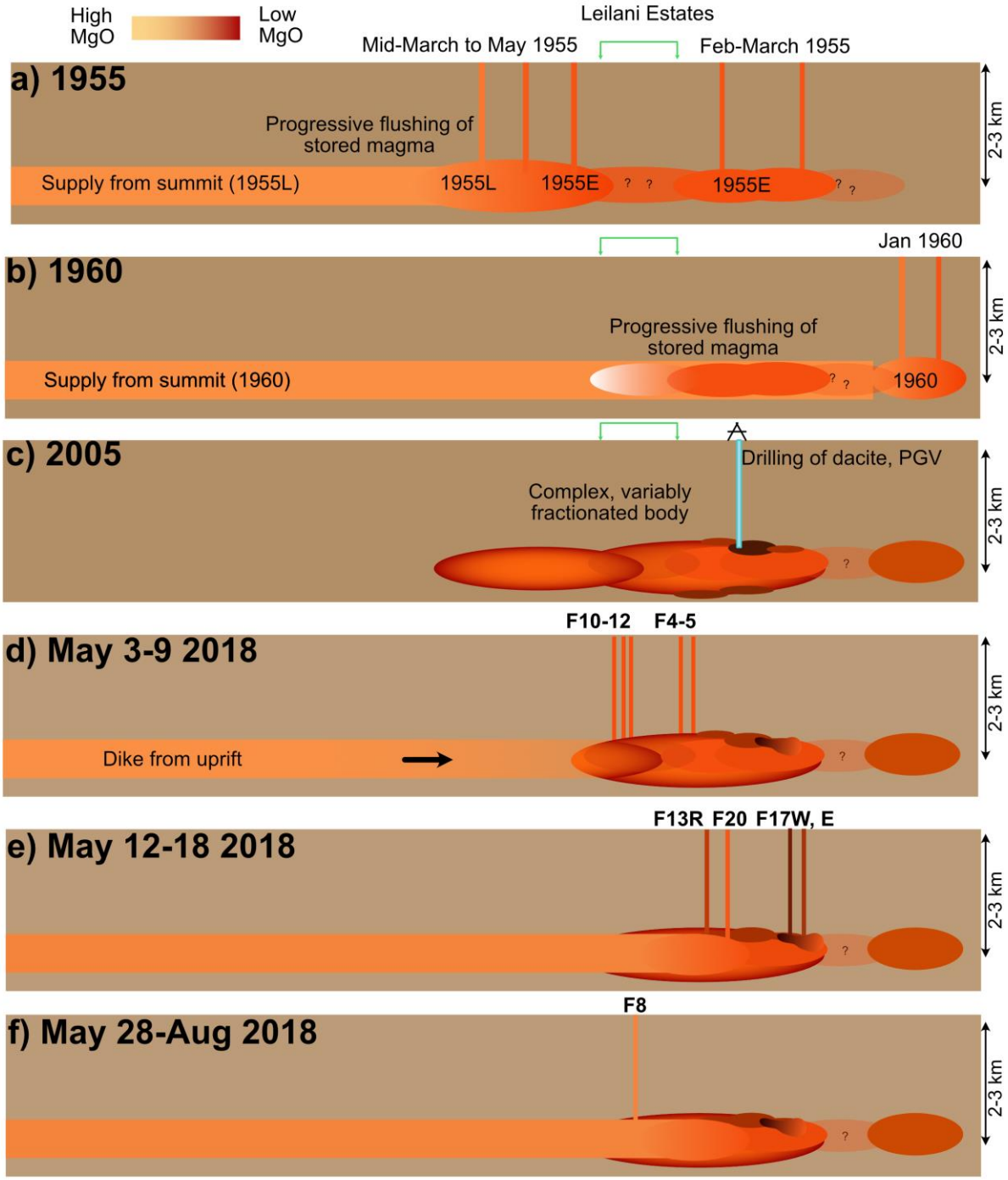

Figure 9 – Schematic diagram showing evolution of the LERZ in the vicinity of the 2018 eruption site. A) More MgO-poor stored melts (1955E) erupt between Feb-March 1955 very close to the 2018 eruption sites (Fig. 1c). More MgO-rich melts (1955L) erupt slightly uprift in mid-March to May. B) Activity farther down the rift zone in 1960 initiates with the eruption of more MgO-poor (1955-like) melts, followed by flushing by more MgO-rich summit magma. C) Hydrothermal drilling in 2005 taps a dacitic body, likely located on the periphery of a complex, variably fractionated magma body. D) Hydraulic pressure from a dike propagating downrift from Pu‘u‘ō‘ō forces stored melts to the

surface. E) Progressively, this dike-supplied material begins to mix with stored melts, until by May 28th, this new component dominates.

Acknowledgements

PW acknowledges funding from a NERC DTP studentship (NE/ L002507/1), a NERC Edinburgh Ion Microprobe Facility grant (IMF675/1118), and a Cambridge University Leave to Work away grant. PA acknowledges funding for development of alphaMELTS for MATLAB by NSF through grant EAR-1947616. We also acknowledge support from the National Science Foundation ICER-20-26904, granted to OFM Research (PI. Ghiorso) for maintaining the ENKI server used to perform VESIcal calculations. PW thanks Matthew Gleeson for help running MELTS for MATLAB, including providing access to his high-powered desktop. PW thanks Iris Buisman and Guilio Lampronti for help collecting EPMA and SEM data for this study, Rod Kindel for the intrepid hike to Fissures 10, 11 and 12 in his backyard, Sarah Allen for help sampling these fissures, and Evgenia Ilyinskaya for coordinating the 2018 and 2019 field campaign. We thank Emily Johnson and two anonymous reviewers, along with associate editor Ken Rubin for very helpful and detailed comments which greatly improved this manuscript.

Data has been archived on Zenodo (https://zenodo.org/badge/latestdoi/417367063) and on Github (where example MELTS for Matlab codes are also provided- https://github.com/PennyWieser/G3-Kil2018-Evolved-MIs).

Bibliography

Antoshechkina, P., Ghiorso, M.S., 2018. MELTS for MATLAB: A new educational and research tool for computational thermodynamics. AGU.

Bauer, G.R., Fodor, R.V., Husler, J.W., Keil, K., 1973. Contributions to the mineral chemistry of Hawaiian rocks: III. Composition and mineralogy of a new rhyodacite occurrence on Oahu, Hawaii. Contr. Mineral. and Petrol. 40, 183–194. https://doi.org/10.1007/BF00373783

Cooper, K.M., Reid, M.R., Murrell, M.T., Clague, D.A., 2001. Crystal and magma residence at Kilauea Volcano, Hawaii: 230Th–226Ra dating of the 1955 east rift eruption. Earth and Planetary Science Letters 184, 703–718. https://doi.org/10.1016/S0012-821X(00)00341-1

Cooper, P., Dustman, M., 1995. Geothermal research, monitoring and testing: final report, geophysics subtask, microseismicity study. Seismological Research Letters.

Danyushevsky, L.V., Plechov, P., 2011. Petrolog3: Integrated software for modeling crystallization processes. Geochemistry, Geophysics, Geosystems 12, n/a-n/a. https://doi.org/10.1029/2011GC003516

Elders, W.A., Friðleifsson, G.Ó., Zierenberg, R.A., Pope, E.C., Mortensen, A.K., Guðmundsson, Á., Lowenstern, J.B., Marks, N.E., Owens, L., Bird, D.K., Reed, M., Olsen, N.J., Schiffman, P., 2011. Origin of a rhyolite that intruded a geothermal well while drilling at the Krafla volcano, Iceland. Geology 39, 231–234. https://doi.org/10.1130/G31393.1

Gaetani, G.A., O'Leary, J.A., Shimizu, N., Bucholz, C.E., Newville, M., 2012. Rapid reequilibration of H2O and oxygen fugacity in olivine-hosted melt inclusions. Geology 40, 915–918. https://doi.org/10.1130/G32992.1

966 Gansecki, C., Lee, R.L., Shea, T., Lundblad, S.P., Hon, K., Parcheta, C., 2019. The tangled tale of
967 Kīlauea's 2018 eruption as told by geochemical monitoring. Science 366, eaaz0147.
968 https://doi.org/10.1126/science.aaz0147

969 Garcia, M.O., Pietruszka, A.J., Norman, M.D., Rhodes, J.M., 2021. Kīlauea's Pu'u 'Ō'ō Eruption (1983–
970 2018): A synthesis of magmatic processes during a prolonged basaltic event. Chemical Geology 581,
971 120391. https://doi.org/10.1016/j.chemgeo.2021.120391

972 Geist, D., Harpp, K., Oswald, P., Wallace, P., Bindeman, I., Christensen, B., 2021. Hekla Revisited:
973 Fractionation of a Magma Body at Historical Timescales. Journal of Petrology 62, egab001.
974 https://doi.org/10.1093/petrology/egab001

975 Gerlach, T.M., McGee, K.A., Elias, T., Sutton, A.J., Doukas, M.P., 2002. Carbon dioxide emission rate
976 of Kīlauea Volcano: Implications for primary magma and the summit reservoir. Journal of
977 Geophysical Research: Solid Earth 107, ECV 3-1-ECV 3-15. https://doi.org/10.1029/2001JB000407

978 Ghiorso, M.S., Gualda, G.A.R., 2015. An H2O–CO2 mixed fluid saturation model compatible with
979 rhyolite-MELTS. Contrib Mineral Petrol 169, 53. https://doi.org/10.1007/s00410-015-1141-8

980 Giordano, D., Russell, J.K., Dingwell, D.B., 2008. Viscosity of magmatic liquids: A model. Earth and
981 Planetary Science Letters 271, 123–134. https://doi.org/10.1016/j.epsl.2008.03.038

982 Gonnermann, H.M., Manga, M., 2013. Chapter 4 - Dynamics of magma ascent in the volcanic
983 conduit, in: Modelling Volcanic Processses. The Physics and Mathmatics of Volcanism.

984 Greaney, A.T., Rudnick, R.L., Helz, R.T., Gaschnig, R.M., Piccoli, P.M., Ash, R.D., 2017. The behavior of
985 chalcophile elements during magmatic differentiation as observed in Kilauea Iki lava lake, Hawaii.
986 Geochimica et Cosmochimica Acta 210, 71–96. https://doi.org/10.1016/j.gca.2017.04.033

987 Gualda, G.A.R., Ghiorso, M.S., Lemons, R.V., Carley, T.L., 2012. Rhyolite-MELTS: a Modified
988 Calibration of MELTS Optimized for Silica-rich, Fluid-bearing Magmatic Systems. Journal of Petrology
989 53, 875–890. https://doi.org/10.1093/petrology/egr080

990 Helz, R.T., 2008. How to Produce Dacitic Melt at Kilauea: Evidence from Historic Kilauea Lava.
991 Presented at the AGU.

992 Helz, R.T., 1980. Crystallization history of Kilauea Iki lava lake as seen in drill core recovered in 1967–
993 1979. Bull Volcanol 43, 675–701. https://doi.org/10.1007/BF02600365

994 Helz, R.T., Thornber, C.R., 1987. Geothermometry of Kilauea Iki lava lake, Hawaii. Bulletin of
995 Volcanology 49, 651–668. https://doi.org/10.1007/BF01080357

996 Helz, R.T., Wright, T.L., 1992. Differentiation and magma mixing on Kilauea's east rift zone: A further
997 look at the eruptions of 1955 and 1960. Part I. The late 1955 lavas. Bulletin of Volcanology 54, 361–
998 384. https://doi.org/10.1007/BF00312319

999 Holcomb, R.T., 1987. Eruptive History and Long-Term Behavoir of Kilauea Volcano.

1000 Houghton, B.F., Gonnermann, H.M., 2008. Basaltic explosive volcanism: Constraints from deposits
1001 and models. Geochemistry 68, 117–140. https://doi.org/10.1016/j.chemer.2008.04.002

1002 Houghton, B.F., Taddeucci, J., Andronico, D., Gonnermann, H.M., Pistolesi, M., Patrick, M.R., Orr,
1003 T.R., Swanson, D.A., Edmonds, M., Gaudin, D., Carey, R.J., Scarlato, P., 2016. Stronger or longer:

1004 Discriminating between Hawaiian and Strombolian eruption styles. Geology 44, 163–166.
1005 https://doi.org/10.1130/G37423.1

1006 Iacovino, K., Matthews, S., Wieser, P.E., Moore, G., Begue, F., 2021. VESIcal Part I: An open-source
1007 thermodynamic model engine for mixed volatile (H2O-CO2) solubility in silicate melt. Earth and
1008 Space Science. https://doi.org/10.1029/2020EA001584

1009 Jaupart, C., Vergniolle, S., 1988. Laboratory models of Hawaiian and Strombolian eruptions. Nature
1010 333, 58–60.

1011 Jenner, F.E., Hauri, E.H., Bullock, E.S., König, S., Arculus, R.J., Mavrogenes, J.A., Mikkelson, N.,
1012 Goddard, C., 2015. The competing effects of sulfide saturation versus degassing on the behavior of
1013 the chalcophile elements during the differentiation of hydrous melts. Geochemistry, Geophysics,
1014 Geosystems 16, 1490–1507. https://doi.org/10.1002/2014GC005670

1015 Johnson, E.A., Rossman, G.R., 2013. The diffusion behavior of hydrogen in plagioclase feldspar at
1016 800-1000 C: Implications for re-equilibration of hydroxyl in volcanic phenocrysts. American
1017 Mineralogist 98, 1779–1787. https://doi.org/10.2138/am.2013.4521

1018 Jónasson, K., 2007. Silicic volcanism in Iceland: Composition and distribution within the active
1019 volcanic zones. Journal of Geodynamics 43, 101–117. https://doi.org/10.1016/j.jog.2006.09.004

1020 Kenedi, C., Shalev, E., Lucas, A., Malin, P., 2010. Microseismicity and 3-D Mapping of an Active
1021 Geothermal Field, Kilauea Lower East Rift Zone, Puna, Hawaii. Presented at the Proceedings World
1022 Geothermal Congress 2010.

1023 Kent, G.M., Singh, S.C., Harding, A.J., Sinha, M.C., Orcutt, J.A., Barton, P.J., White, R.S., Bazin, S.,
1024 Hobbs, R.W., Tong, C.H., Pye, J.W., 2000. Evidence from three-dimensional seismic re¯ectivity images
1025 for enhanced melt supply beneath mid-ocean -ridge discontinuities 406, 5.

1026 Koleszar, A.M., Saal, A.E., Hauri, E.H., Nagle, A.N., Liang, Y., Kurz, M.D., 2009. The volatile contents of
1027 the Galapagos plume; evidence for H2O and F open system behavior in melt inclusions. Earth and
1028 Planetary Science Letters 287, 442–452. https://doi.org/10.1016/j.epsl.2009.08.029

1029 Lerner, A.H., Wallace, P., Shea, T., 2021. The petrologic and degassing behavior of sulfur and other
1030 magmatic volatiles from the 2018 eruption of Kīlauea, Hawai'i: melt concentrations, magma storage
1031 depths, and magma recycling. Bulletin Volcanology 83:43, 1–32.

1032 Llewellin, E.W., Mader, H.M., Wilson, S.D.R., 2002. The rheology of a bubbly liquid. Proc. R. Soc.
1033 Lond. A 458, 987–1016. https://doi.org/10.1098/rspa.2001.0924

1034 Lowenstern, J., 2001. Carbon dioxide in magmas and implications for hydrothermal systems.
1035 Mineralium Deposita 36, 490–502. https://doi.org/10.1007/s001260100185

1036 Macdonald, G.A., 1962. The 1959 and 1960 eruptions of Kilauea volcano, Hawaii, and the
1037 construction of walls to restrict the spread of the lava flows. Bull Volcanol 24, 249–294.
1038 https://doi.org/10.1007/BF02599351

1039 Manga, M., Loewenberg, M., 2001. Viscosity of magmas containing highly deformable bubbles.
1040 Journal of Volcanology and Geothermal Research 105, 19–24. https://doi.org/10.1016/S0377-
1041 0273(00)00239-0

1042 Marske, J.P., 2010. Magmatic History Of Lavas from Kīlauea Volcano, Hawai'I and South Pagan
1043 Volcano, Northern Mariana Islands. PhD Thesis, UH Manoa.

1044 Masotta, M., Mollo, S., Nazzari, M., Tecchiato, V., Scarlato, P., Papale, P., Bachmann, O., 2018.
1045 Crystallization and partial melting of rhyolite and felsite rocks at Krafla volcano: A comparative
1046 approach based on mineral and glass chemistry of natural and experimental products. Chemical
1047 Geology 483, 603–618. https://doi.org/10.1016/j.chemgeo.2018.03.031

1048 Mbia, P., Mortensen, A., Oskarsson, N., Hardarson, B., 2015. Sub-surface geology, petrology and
1049 hydrothermal alteration of the Menengai geothermal field, Kenya: Case study of wells MW-02, MW-
1050 04, MW-06 and MW-07. Presented at the World Geothermal Congress 2015.
1051 https://www.geothermal-energy.org/pdf/ IGAstandard/WGC/2015/12071.pdf.

1052 Moore, R.B., 1992. Volcanic geology and eruption frequency, lower east rift zone of Kilauea volcano,
1053 Hawaii. Bulletin of Volcanology 54, 475–483. https://doi.org/10.1007/BF00301393

1054 Mortensen, A.K., Gronvold, K., Gudmundsson, A., Steingrimsson, B., Egilson, T., 2010. Quenched
1055 Silicic Glass from Well KJ-39 in Krafla, North-Eastern Iceland, in: Proceedings World Geothermal
1056 Congress 2010, Bali, Indonesia, 25-29 April 2010.

1057 Moussallam, Y., Edmonds, M., Scaillet, B., Peters, N., Gennaro, E., Sides, I., Oppenheimer, C., 2016.
1058 The impact of degassing on the oxidation state of basaltic magmas: A case study of Kīlauea volcano.
1059 Earth and Planetary Science Letters 450, 317–325. https://doi.org/10.1016/j.epsl.2016.06.031

1060 Neal, C.A., Brantley, S.R., Antolik, L., Babb, J.L., Burgess, M., Calles, K., Cappos, M., Chang, J.C.,
1061 Conway, S., Desmither, L., Dotray, P., Elias, T., Fukunaga, P., Fuke, S., Johanson, I.A., Kamibayashi, K.,
1062 Kauahikaua, J., Lee, R.L., Pekalib, S., Miklius, A., Million, W., Moniz, C.J., Nadeau, P.A., Okubo, P.,
1063 Parcheta, C., Patrick, M.R., Shiro, B., Swanson, D.A., Tollett, W., Trusdell, F., Younger, E.F., Zoeller,
1064 M.H., Montgomery-Brown, E.K., Anderson, K.R., Poland, M.P., Ball, J.L., Bard, J., Coombs, M.,
1065 Dietterich, H.R., Kern, C., Thelen, W.A., Cervelli, P.F., Orr, T., Houghton, B.F., Gansecki, C., Hazlett, R.,
1066 Lundgren, P., Diefenbach, A.K., Lerner, A.H., Waite, G., Kelly, P., Clor, L., Werner, C., Mulliken, K.,
1067 Fisher, G., Damby, D., 2018. The 2018 rift eruption and summit collapse of Kīlauea Volcano. Science
1068 eaav7046. https://doi.org/10.1126/science.aav7046

1069 Neave, D.A., Hartley, M.E., Maclennan, J., Edmonds, M., Thordarson, T., 2017. Volatile and light
1070 lithophile elements in high-anorthite plagioclase-hosted melt inclusions from Iceland. Geochimica et
1071 Cosmochimica Acta 205, 100–118. https://doi.org/10.1016/j.gca.2017.02.009

1072 Norman, M., 2005. Trace-element distribution coefficients for pyroxenes, plagioclase, and olivine in
1073 evolved tholeiites from the 1955 eruption of Kilauea Volcano, Hawai'i, and petrogenesis of
1074 differentiated rift-zone lavas. American Mineralogist 90, 888–899.
1075 https://doi.org/10.2138/am.2005.1780

1076 Parfitt, E.A., Wilson, L., 1995. Explosive volcanic eruptions-IX. The transition between Hawaiian-style
1077 lava fountaining and Strombolian explosive activity. Geophysical Journal International 121, 226–232.
1078 https://doi.org/10.1111/j.1365-246X.1995.tb03523.x

1079 Patrick, M.R., Dietterich, H.R., Lyons, J.J., Diefenbach, A.K., Parcheta, C., Anderson, K.R., Namiki, A.,
1080 Sumita, I., Shiro, B., Kauahikaua, J.P., 2019. Cyclic lava effusion during the 2018 eruption of Kīlauea
1081 Volcano. Science 366, eaay9070. https://doi.org/10.1126/science.aay9070

1082 Patrick, M.R., Houghton, B.F., Anderson, K.R., Poland, M.P., Montgomery-Brown, E., Johanson, I.,
1083 Thelen, W., Elias, T., 2020. The cascading origin of the 2018 Kīlauea eruption and implications for
1084 future forecasting. Nat Commun 11, 5646. https://doi.org/10.1038/s41467-020-19190-1

Pietruszka, A.J., Garcia, M.O., 1999a. A Rapid Fluctuation in the Mantle Source and Melting History of Kilauea Volcano Inferred from the Geochemistry of its Historical Summit Lavas (1790–1982). Journal of Petrology 40, 1321–1342.

Pietruszka, A.J., Garcia, M.O., 1999b. The size and shape of Kilauea Volcano's summit magma storage reservoir: a geochemical probe. Earth and Planetary Science Letters 167, 311–320. https://doi.org/10.1016/S0012-821X(99)00036-9

Pietruszka, A.J., Garcia, M.O., Rhodes, J.M., 2021. Accumulated Puʻu ʻŌʻō magma fed the voluminous 2018 rift eruption of Kīlauea Volcano: evidence from lava chemistry. Bull Volcanol 83, 59. https://doi.org/10.1007/s00445-021-01470-3

Pietruszka, A.J., Heaton, D.E., Marske, J.P., Garcia, M.O., 2015. Two magma bodies beneath the summit of Kīlauea Volcano unveiled by isotopically distinct melt deliveries from the mantle. Earth and Planetary Science Letters 413, 90–100. https://doi.org/10.1016/j.epsl.2014.12.040

Portnyagin, M., Almeev, R., Matveev, S., Holtz, F., 2008. Experimental evidence for rapid water exchange between melt inclusions in olivine and host magma. Earth and Planetary Science Letters 272, 541–552. https://doi.org/10.1016/j.epsl.2008.05.020

Rooney, T.O., Hart, W.K., Hall, C.M., Ayalew, D., Ghiorso, M.S., Hidalgo, P., Yirgu, G., 2012. Peralkaline magma evolution and the tephra record in the Ethiopian Rift. Contrib Mineral Petrol 164, 407–426. https://doi.org/10.1007/s00410-012-0744-6

Rooyakkers, Shane M, Stix, J., Berlo, K., Petrelli, M., Hampton, R.L., Barker, S.J., Morgavi, D., 2021. The Origin of Rhyolitic Magmas at Krafla Central Volcano (Iceland). Journal of Petrology 62, egab064. https://doi.org/10.1093/petrology/egab064

Rooyakkers, Shane M., Stix, J., Berlo, K., Petrelli, M., Sigmundsson, F., 2021. Eruption risks from covert silicic magma bodies. Geology. https://doi.org/10.1130/G48697.1

Russell, J.K., Stanley, C., 1990. Origins of the 1954-1960 Lavas, Kilauea Volcano, Hawaii: Major Element Constraints on Shallow Reservoir Magmatic Processe. Journal of Geophysical Research 95, 5021–5047.

Sides, Edmonds, M., Maclennan, J., Houghton, B.F., Swanson, D.A., Steele-MacInnis, M.J., 2014a. Magma mixing and high fountaining during the 1959 Kīlauea Iki eruption, Hawai'i. Earth and Planetary Science Letters 400, 102–112. https://doi.org/10.1016/j.epsl.2014.05.024

Sides, Edmonds, M., Maclennan, J., Swanson, D.A., Houghton, B.F., 2014b. Eruption style at Kīlauea Volcano in Hawai'i linked to primary melt composition. Nature Geoscience 7, 464–469. https://doi.org/10.1038/ngeo2140

Soldati, A., Houghton, B.F., Dingwell, D.B., 2021. A lower bound on the rheological evolution of magmatic liquids during the 2018 Kilauea eruption. Chemical Geology 576, 120272. https://doi.org/10.1016/j.chemgeo.2021.120272

Sparks, S.R.J., Sigurdsson, H., Wilson, L., 1977. Magma mixing: a mechanism for triggering acid explosive eruptions. Nature 267, 315–318. https://doi.org/10.1038/267315a0

Stock, M.J., Geist, D., Neave, D.A., Gleeson, M.L.M., Bernard, B., Howard, K.A., Buisman, I., Maclennan, J., 2020. Cryptic evolved melts beneath monotonous basaltic shield volcanoes in the Galápagos Archipelago. Nat Commun 11, 3767. https://doi.org/10.1038/s41467-020-17590-x

Swanson, D.A., Duffield, W.A., Jackson, D.B., Peterson, D.W., 1979. Chronological narrative of the 1969-71 Mauna Ulu eruption of Kilauea Volcano, Hawaii. Geological Survey Professional Paper 1056.

Teplow, W., Marsh, B., Hulen, 2009. Dacite Melt at the Puna Geothermal Venture Wellfield, Big Island of Hawaii. GRC Transactions 33.

Trusdell, F., Wolfe, E., Morris, J., 2006. Digital Database of the Geologic Map of the Island of Hawai'i. USGS Data Series 144.

Wanless, V.D., Perfit, M.R., Ridley, W.I., Klein, E., 2010. Dacite Petrogenesis on Mid-Ocean Ridges: Evidence for Oceanic Crustal Melting and Assimilation. Journal of Petrology 51, 2377–2410. https://doi.org/10.1093/petrology/egq056

Wieser, P., Iacovino, K., Matthews, S., Moore, G., Allison, C., 2021. VESIcal II - A Critical Approach to Volatile Solubility Modelling using an Open-Source Python3 Engine. EarthArxiv. https://doi.org/10.31223/X5K03T

Wieser, P.E., Edmonds, M., Maclennan, J., Jenner, F.E., Kunz, B.E., 2019. Crystal Scavenging from Mush Piles Recorded by Melt Inclusions. Nature Communications.

Wieser, P.E., Iacovino, K., Matthews, S., 2021a. VESIcal part II.

Wieser, P.E., Jenner, F., Edmonds, M., Maclennan, J., Kunz, B.E., 2020. Chalcophile elements track the fate of sulfur at Kīlauea Volcano, Hawai'i. Geochimica et Cosmochimica Acta S0016703720303239. https://doi.org/10.1016/j.gca.2020.05.018

Wieser, P.E., Lamadrid, H., Maclennan, J., Edmonds, M., Matthews, S., Iacovino, K., Jenner, F.E., Gansecki, C., Trusdell, F., Lee, R.L., Ilyinskaya, E., 2021b. Reconstructing Magma Storage Depths for the 2018 Kīlauean Eruption From Melt Inclusion CO_2 Contents: The Importance of Vapor Bubbles. Geochem Geophys Geosyst 22. https://doi.org/10.1029/2020GC009364

Wilson, L., Head, J.W., 1981. Ascent and eruption of basaltic magma on the Earth and Moon. J. Geophys. Res. 86, 2971–3001. https://doi.org/10.1029/JB086iB04p02971

Wright, T.L., Fiske, R.S., 1971. Origin of the Differentiated and Hybrid Lavas of Kilauea Volcano, Hawaii. Journal of Petrology 12, 1–65. https://doi.org/10.1093/petrology/12.1.1

Wright, T.L., Peck, D.L., Shaw, H.R., 1976. Kilauea Lava Lakes: Natural Laboratories for Study of Cooling, Crystallization, and Differentiation of Basaltic Magma, in: Sutton, G.H., Manghnani, M.H., Moberly, R., Mcafee, E.U. (Eds.), Geophysical Monograph Series. American Geophysical Union, Washington, D. C., pp. 375–390. https://doi.org/10.1029/GM019p0375

Zoeller, M.H., Perroy, R.L., Wessels, R., Fisher, G.B., Robinson, J.E., Bard, J.A., Peters, J., Mosbrucker, A., Parcheta, C.E., 2020. Geospatial database of the 2018 lower East Rift Zone eruption of Kilauea Volcano, Hawaii. https://doi.org/10.5066/P9S7UQKQ